Digital Comprehensive Summaries of Uppsala Dissertations
from the Faculty of Science and Technology 2571

Water in Prussian blue analogues

A blessing or a curse?

IDA NIELSEN

ACTA UNIVERSITATIS
UPSALIENSIS
2025

ISSN 1651-6214
ISBN 978-91-513-2558-3
urn:nbn:se:uu:diva-565121

UPPSALA
UNIVERSITET

Dissertation presented at Uppsala University to be publicly examined in Siegbahnsalen, Ångströmlaboratoriet, Regementsvägen 10, Uppsala, Friday, 3 October 2025 at 09:15 for the degree of Doctor of Philosophy. The examination will be conducted in English. Faculty examiner: Professor Andrew Goodwin (University of Oxford).

Abstract

Nielsen, I. 2025. Water in Prussian blue analogues. A blessing or a curse? *Digital Comprehensive Summaries of Uppsala Dissertations from the Faculty of Science and Technology* 2571. 63 pp. Uppsala: Acta Universitatis Upsaliensis. ISBN 978-91-513-2558-3.

Prussian blue analogues (PBAs), $A_xM[M'(CN)_6]_{1-y}\cdot z$G, are used in many different applications, such as energy storage, due to their tunable composition and structural diversity. To understand the material properties, it is important to accurately determine the composition and atomic structure of these materials. However, this is challenging due to the interdependent relationship between the three compositional parameters: the alkali cation (A_x), water (z), and $[M'(CN)_6]^{n-}$ (y) vacancy content. Furthermore, the atomic structure depends on the composition, which leads to a rich structural landscape that further influences the material properties. This thesis presents a comprehensive strategy for characterizing the composition and atomic structure of iron- and sodium-based PBAs. To accurately determine the composition of iron-based PBAs, it was found that a combination of multiple characterization techniques is needed; especially Mössbauer spectroscopy proved vital for accurately determining the vacancy content. Neutron diffraction, neutron total scattering, quasi-elastic neutron scattering, and inelastic neutron scattering were applied to probe the local and average structures as well as the dynamics of the water in PBAs as a function of sodium content and temperature. It was found that the PBA system is more dynamic than previously thought, and that the sodium and water can occupy a broad range of positions, which change with temperature. The material becomes more disordered upon dehydration or when the sodium content is lowered. Additionally, distortions of the PBA framework proved to be an inherent property of these materials. This work also demonstrates that neutron diffraction alone is insufficient to describe sodium and water positions, confirming the need for local probes such as total scattering and inelastic neutron scattering. These findings highlight the importance of proper compositional, structural, and dynamical characterization using multiple techniques and lay the groundwork for further development of new PBAs.

Keywords: Prussian blue analogues, neutron scattering, sodium-ion batteries, crystallography, spectroscopy, structural dynamics.

Ida Nielsen, Department of Chemistry - Ångström, Structural Chemistry, Box 538, Uppsala University, SE-751 21 Uppsala, Sweden.

ISSN 1651-6214
ISBN 978-91-513-2558-3
URN urn:nbn:se:uu:diva-565121 (http://urn.kb.se/resolve?urn=urn:nbn:se:uu:diva-565121)

Til Lya ♡

List of papers

This thesis is based on the following papers, which are referred to in the text by their Roman numerals.

I D. Boras,* **Ida Nielsen,*** A. Buckel, T. Ericsson, L. Häggström, R. Younesi, T. Stabb, W. R. Brant. Determining internal porosity in Prussian blue analogue cathode materials using positron annihilation lifetime spectroscopy. *J. Mater. Sci. 2023, 58, 16344-16356.*
*The authors contributed equally to the work.

II **Ida Nielsen,** Dj. Dzodan, D. O. Ojwang, P. F. Henry, A. Ulander, G. Ek, L. Häggström, T. Ericsson, H. L. B. Boström, W. R. Brant. Water driven phase transitions in Prussian white cathode materials. *J. Phys. Energy 2022, 4, 044012.*

III **Ida Nielsen,** M. Eremenko, Y. Zhang, M. G. Tucker, W. R. Brant. Local structure of hydrated and dehydrated Prussian white cathode materials. *Submitted.*

IV **Ida Nielsen,** A. Ulander, F. Juranyi, S. R. Larsen, M. Karlsson, W. R. Brant, M. S. Andersson. Impact of sodium on the water dynamics in Prussian blue analogues. *Chem. Mater. 2024, 36, 22, 11246-11253.*

V **Ida Nielsen,** Y. Cheng, F. Schwarz, A. Mace, H. Cavaye, J. Armstrong, M. G. Tucker, M. Karlsson, W. R. Brant, M. S. Andersson. Vibrational water dynamics in sodium-based Prussian blue analogues. *Submitted.*

VI **Ida Nielsen,** C. A. Hall, A-M. Mattsson, R. Younesi, A. Buckel, G. Ek, W. R. Brant. Unravelling the origin of capacity fade in Prussian white hard carbon full cells through *operando* X-ray diffraction. *J. Mater. Chem. A. 2024, 12, 17413-17421.*

Disclaimer: Parts of this thesis are based on my licentiate thesis entitled *New strategies for characterizing Prussian blue analogues* (Uppsala University, 2023).

Comments on the author's contributions to the papers.

I Performed the characterization and data analysis for all samples using X-ray diffraction, thermogravimetric analysis, inductively coupled plasma-optical emission spectroscopy, and scanning electron microscopy. Wrote the manuscript with input from co-authors.

II Performed all data analysis. Wrote the manuscript with input from co-authors.

III Planned and performed all the experimental work except for the sample preparation and Mössbauer spectroscopy. Performed all data analysis. Wrote the manuscript with input from co-authors.

IV Planned and performed all the experimental work except for the sample preparation and Mössbauer spectroscopy. Performed all data analysis. Wrote the manuscript with input from co-authors.

V Planned and performed all the experimental work except for the sample preparation and Mössbauer spectroscopy. Performed all data analysis except for the theoretical calculations. Wrote the manuscript with input from co-authors.

VI Planned and performed all the experimental work except for cell assembly and pre-cycling. Performed all data analysis. Wrote the manuscript with input from co-authors.

Papers not included in the thesis

The author contributed to the following papers that are not included in the thesis.

i C. L. Jakobsen, M. Johansen, T. Ericsson, L. Häggström, C. K. Christensen, **Ida Nielsen,** W. R. Brant, D. B. Ravnsbæk. Ion-intercalation mechanism and structural relaxation in layered iron phosphate $Na_3Fe_3(PO_4)_4$ cathodes. *Front. Mater. Electrochem. 2024, 3:1433241.*

ii H. Chen, A-M. Mattsson, L. King, H. Liu, **Ida Nielsen,** T. Ericson, A. Preobrajenski, W. R. Brant, M. Halin. Study of degradation mechanisms in aqueous-processed Ni-rich cathodes for enhanced sustainability of batteries. *J. Mater. Chem A. 2024, 12, 25393-25406.*

iii A. E. Ulander, **Ida Nielsen,** L. Häggström, W. R. Brant. Concentration effects on co-precipitation synthesis of Prussian white for sodium ion batteries. *In manuscript.*

iv A-M. Mattsson, **Ida Nielsen,** F. Björefors, W. R. Brant. Operando X-ray diffraction and voltammetric analysis of phase transitions in $Li_xNa_yFe[Fe(CN)_6]$. *In manuscript.*

Contents

Abbreviations

A list of the abbreviations used in the thesis.

Abbreviation	**Meaning**
EISF	Elastic incoherent structure factor
f.u.	Formula unit
ICP-OES	Inductively coupled plasma-optical emission spectroscopy
INS	Inelastic neutron scattering
PALS	Positron annihilation lifetime spectroscopy
PBAs	Prussian blue analogues
PDF	Pair distribution function
QENS	Quasi-elastic neutron scattering
RDF	Radial distribution function
RMC	Reverse Monte Carlo
TGA	Thermogravimetric analysis

1. Introduction

1.1 Prussian blue and its analogues

Prussian blue is a mixed-valence iron cyanide compound with the chemical formula $Fe_4^{3+}[Fe^{2+}(CN)_6]_3$ named after its deep blue color and usage as a pigment in the early 18th century [1]. Despite the early discovery, the structure was only first described in 1936 by Keggin and Miles using X-ray diffraction [2]. Prussian blue crystallizes in the cubic space group $Fm\bar{3}m$, where the unit cell is built up by eight subcubes (Figure 1.1). Each subcube consists of eight iron atoms occupying the corners of the subcube linked together by bridging cyanide ligands which creates a porous framework. The cyanide ligands selectively bind *via* carbon to one iron atom, and thus, only nitrogen to the second iron atom. This specific coordination of the cyanide ligands to iron is what gives rise to the face-centered structure [3]. The selective bonding is also shown in the chemical formula by having the carbon-bound iron atom inside the square brackets. Prussian blue has a very porous structure due to the 25% stoichiometric deficiency of $[Fe(CN)_6]^{4-}$ units relative to the nitrogen-bound iron. The large cavities created by the vacancies can be occupied by a range of small molecules, but are most commonly occupied by water molecules that are either hydrogen-bonded to other water molecules inside the cavities or coordinated to the nitrogen-bound iron atoms to fulfill the coordination sphere of iron [4].

The arrangement of carbon and nitrogen in the cubic $Fm\bar{3}m$ structure of Prussian blue results in the iron atoms having different electronic structures [3]. The difference in the electronic structure of the two iron atoms is related to which end of the cyanide ligand is coordinated to iron. When carbon is bound to iron, electrons from carbon are donated into the iron *d*-orbitals *via* a σ-bond. The filled *d*-orbitals on the iron atom then donate electrons back into an empty π^*-orbital in the cyanide ligand *via* the carbon atom. The strong π-backbonding effect results in a large splitting of the *d*-orbitals of the carbon-bound iron leading to a low-spin electron configuration for Fe_C^{2+} (Figure 1.1a). On the other hand, the nitrogen atom of the cyanide ligand is a strong σ-donor resulting in a smaller splitting of the *d*-orbitals relative to that of the *d*-orbitals on the carbon-bound iron atom. The smaller splitting of the *d*-orbitals results in a high-spin electron configuration for Fe_N^{3+}. The deep blue color of Prussian blue originates from an intervalence charge transfer from Fe_C^{2+} to Fe_N^{3+} that absorbs orange-red light in the visible spectrum. By changing the oxidation states of the iron atoms

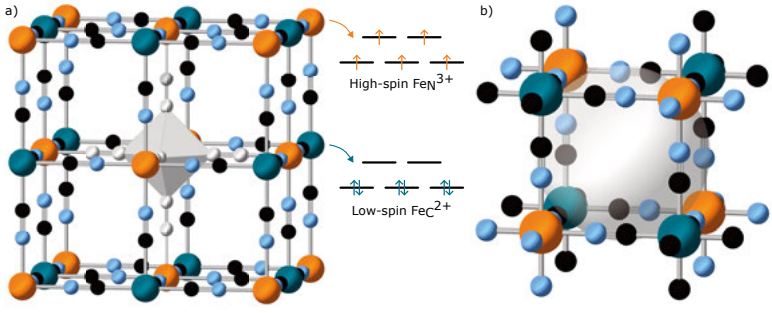

Figure 1.1. a) The structure of Prussian blue consists of two octahedrally coordinated iron atoms (with their respective electronic configuration) linked by cyanide ligands *via* the corners of the octahedra. The presence of $[Fe(CN)_6]^{4-}$ vacancies in the structure is represented by the grey octahedra, while the missing atoms are represented by grey spheres. b) The cavity within a subcube (shown as a transparent grey sphere covering the window faces as well) can be occupied by alkali cations (A^+) and/or neutral guest molecules (G).

in Prussian blue, compounds with different colors, such as white and green, can be obtained [3].

The compositional versatility of Prussian blue, and hence the existence of a large number of Prussian blue-related compounds, comes from the possibility to substitute iron with other transition metals and to incorporate different alkali cations into the porous framework in addition to water molecules (Figure 1.1b). Due to the high stability of the $[Fe(CN)_6]^{4-}$ unit, it is typically the nitrogen-bound iron atom that is substituted with another transition metal [3]. However, in rare cases, the carbon-bound iron atom can be substituted as well. All these compounds are referred to as Prussian blue analogues (PBAs) whose chemical formula can be described as $A_xM[M'(CN)_6]_{1-y}{\cdot}zG$, where A is an alkali cation, M and M' are transition metals, y denotes hexacyanometallate $[M'(CN)_6]^{n-}$ vacancies, and G is a neutral guest species such as water. The compositional variability leads to PBAs being used in a broad range of applications such as biomedical applications, electrode materials in batteries, magnetic applications, catalysis, and gas adsorption [5–9].

1.2 Iron-based Prussian blue analogues

While it is possible to make many different PBAs, the majority of studies are focused on hexacyanoferrates. This is because the material contains cyanide, which, if released from the metal complex, can hydrolyze to form toxic hydrogen cyanide gas. Cyanide binds more strongly to iron than many other transition metals, leading to frameworks that are structurally stable [10]. Consequently, the compounds consisting of $A_xM[Fe(CN)_6]_{1-y}$ are very

stable, and thus, safe to handle. Using iron in PBAs also has other advantages, such as iron's relative abundance and the simplicity of the synthesis conditions required to make iron-based PBAs [3]. This thesis specifically investigates the PBAs where both transition metals are iron. PBAs can, in general, accommodate a wide range of alkali cations *e.g.,* Li^+, Na^+, K^+, Rb^+, and Cs^+ [11]. The choice of sodium in this work is based on the PBA's application as a positive electrode material in sodium-ion batteries.

The PBAs investigated in this thesis can be described by the chemical formula $Na_{2-4y-x}Fe[Fe(CN)_6]_{1-y}\cdot zH_2O$. The formula differs from the above introduced general PBA formula as it describes the correlations between the three compositional parameters x, y, and z that exist for iron-based PBAs. The maximum amount of sodium that can be included in the structure is determined by the oxidation state of the two iron atoms. Since it is unlikely that iron will adopt an oxidation state lower than 2+, the upper limit for the sodium content is two per formula unit (f.u.) when $y = 0$ and both iron atoms are 2+. As both iron atoms can be oxidized to 3+, the sodium content can vary accordingly, ranging from fully sodiated to fully desodiated, giving the limiting range of $0 \leq x \leq 2$. The total sodium content that can be included in the structure also depends on the $[Fe(CN)_6]^{n-}$ vacancy content. For example, if starting from $Fe^{3+}[Fe^{3+}(CN)_6]$, removal of one $[Fe(CN)_6]^{3-}$ unit results in one less sodium ion that can be included. Furthermore, an additional three Fe^{3+} ions must be reduced to Fe^{2+} to counteract the loss of the 3- charge of the lost $[Fe(CN)_6]^{3-}$ complex. This results in four fewer sodium ions that can be included in the structure. Since the loss of one $[Fe(CN)_6]^{3-}$ unit results in a total of four changed iron atoms (one complex missing and three reduced iron atoms), the impact of vacancies on the sodium content is $-4y$. The vacancy content can in principle be between $0 \leq y \leq 0.5$, however, vacancy contents of 25-30% are commonly observed [12, 13]. Since the synthesis of these materials happens in water, the resulting compounds contain water. As for the sodium content, the water content is also strongly affected by the number of vacancies. In general, the more porous the material (vacancy-rich), the more water can occupy the large cavities, while vacancy-free materials contain less water. In the presence of smaller alkali cations, such as lithium and sodium, there is still space for water to occupy, while for larger cations, the possibility for including water decreases [11, 14]. As will be discussed later in this thesis, the sodium and water content appear to be correlated [15].

The composition of PBAs is complex, and the complexity of the material is also increased by the fact that the structure varies as a function of the composition (Figure 1.2) [11]. The fully sodiated ($x = 0$), vacancy-free ($y = 0$), hydrated material, $Na_2Fe[Fe(CN)_6]\cdot zH_2O$, adopts monoclinic $P2_1/n$ symmetry, while for sodium contents below ~1.2 per f.u., the material has cubic $Fm\bar{3}m$ symmetry [11]. According to a meta-study of the PBA literature, there exists a compositional region that lies between a sodium content of

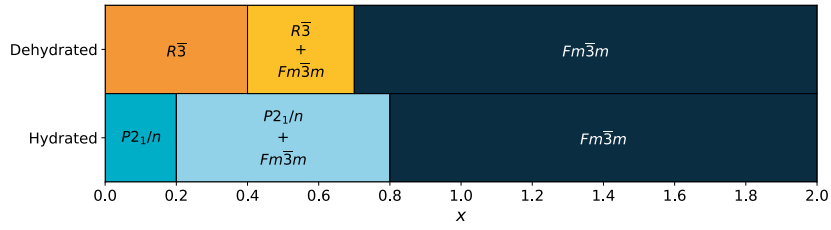

Figure 1.2. Phase diagram for $Na_{2-x}Fe[Fe(CN)_6]\cdot zH_2O$ as a function of the sodium and water content.

$0.2 < x < 0.8$ and a vacancy content between $0 < y < 0.2$, where no phase pure materials have been reported [11]. Thus, for compositions where there are 1.2-1.8 sodium ions per f.u., the material consists of both monoclinic $P2_1/n$ and cubic $Fm\bar{3}m$ phases. The dehydrated material obtains rhombohedral $R\bar{3}$ symmetry at high sodium contents, which converts to cubic $Fm\bar{3}m$ symmetry upon sodium removal. The two-phase region lies between a sodium content of $0.4 < x < 0.7$ [16]. Iron-based PBAs with a vacancy content of $y > 0.2$ generally result in undistorted structures with cubic $Fm\bar{3}m$ symmetry as traditional Prussian blue [11]. However, it is hard to tell what specific vacancy level gives rise to distorted *vs* undistorted structures since the alkali cation and vacancy content are correlated, and it is hard to obtain synthetic control over the vacancy content.

1.3 The role of water

The material in focus in this thesis is the iron-based, vacancy-free ($y = 0$) PBA described by the general formula $Na_{2-x}Fe[Fe(CN)_6]\cdot zH_2O$. Sodium-rich PBAs exhibit rich structural diversity due to structural distortions, which depend on the composition. With different structures for different compositions, phase transitions are unavoidable. This is also the case for the PBA of interest in this thesis, where the structure changes as a function of the sodium and water content. Due to the negative effects of using the hydrated material as an electrode material in non-aqueous batteries, *e.g.,* side reactions, ion transport hindrance, and gas formation [17, 18], the water is removed from the structure before use. However, dehydration induces an 18% volume contraction resulting in particle cracking and strain [16]. Moreover, in the absence of water, the structure of the material changes between rhombohedral $R\bar{3}$ and cubic $Fm\bar{3}m$ phases during sodium extraction and insertion (Figure 1.2). This also coincides with large changes in the volume ($\pm$17%) leading to loss of capacity and poor cycling stability during long-term cycling [16, 19]. This large change in volume is not observed during the desodiation of the hydrated material. In fact, the presence of water modifies this phase transition preventing the large volume changes from occurring

resulting in improved structural stability during long-term electrochemical cycling due to better support of the PBA framework [20].

The wide phase diagram for cation-rich PBAs is in contrast to most PBAs, which exhibit cubic symmetries [11]. The size of the cation is believed to affect this different behavior; non-cubic symmetries are commonly obtained due to optimized bonding conditions when having smaller cations such as lithium and sodium. The presence of water adds another layer of complexity to this description since there is still space for water to occupy the interstitial and window sites even when smaller cations are present (Figure 1.1b). The role of water on phase transitions is yet to be fully understood, and its investigation has proven challenging. For example, thermogravimetric analysis (TGA) measurements can be dependent on the experimental setup and should be combined with mass spectrometry to fully decouple the mass loss processes [11]. Furthermore, the low X-ray scattering length of light elements and the disordered nature of the water make it hard to determine its position accurately, and hence its role during phase transitions. A PBA meta-study indicated that the presence of water does not induce phase transitions but instead modifies the magnitude of distortions already existing within a given symmetry [11]. To investigate this hypothesis, local probes and other types of radiation, such as neutrons, need to be used to aid the understanding of the role of water in PBAs. This will benefit the understanding of PBAs both from a fundamental and an application point of view.

2. Scope of the thesis

The PBA materials class has proven challenging to characterize, both in terms of composition and atomic structure, which may lead to inconsistencies in the reported properties. In addition, there is limited information about the dynamics of water in PBAs, which is related to how water interacts with the PBA framework and how it affects the phase transitions in the material. This thesis aims to determine the position and dynamics of water in iron-based PBAs as a function of the sodium content and temperature. There is a strong emphasis on applying different techniques and modeling different types of data to get a full picture of the PBAs. The main technique used in this thesis is neutron scattering because of its sensitivity towards lighter elements and the possibility for dynamic information. This work also aims to bridge the gap between experimental data and theoretical calculations to characterize PBAs thoroughly and lay the groundwork for more advanced calculations. Improved calculations of PBAs give higher certainty in the calculated properties, and thus, better guidance in the design of new and improved PBAs tailored for different applications. **Paper I** investigates the techniques necessary to properly characterize the composition of iron-based PBAs, and positron annihilation lifetime spectroscopy is introduced as a possible technique to determine the internal porosity of PBAs. **Paper II-III** study the average and local structure of a sodium-rich, iron-based PBA as a function of the temperature. **Papers IV-V** explore the local dynamics of water and its effect on stabilization of the PBA framework as a function of the sodium content. With the detailed knowledge of the composition, atomic structure, and dynamics of water, **Paper VI** focuses on an applied system looking into volume changes and phase transitions during long-term cycling of a sodium-rich, iron-based PBA in a non-aqueous sodium-ion battery.

3. Methodology

3.1 Materials synthesis

To obtain sodium-rich PBAs with a low $[Fe(CN)_6]^{n-}$ vacancy content, synthetic control is crucial. In this work, the pristine materials have been synthesized from either an acid decomposition or co-precipitation method by collaborators. The two synthesis methods yielded similar material compositions ($Na_2Fe[Fe(CN)_6]\cdot zH_2O$) with particle sizes ranging from 2-30 μm. The Prussian blue sample in Paper I and the samples used in Papers II-III were synthesized in-house. The starting material/electrodes in Papers I and IV-VI were obtained from Altris AB. The PBAs with lower sodium contents in Papers I and IV-V were synthesized using the pristine powder obtained from Altris AB and oxidizing agents of different strengths, *e.g.*, H_2O, I_2, or NO_2BF_4. Details about the syntheses can be found in the experimental methods sections of the respective papers [15, 21, 22]. The obtained materials (except for Prussian blue) are air- and moisture-sensitive, hence all further handling and treatment were performed under an inert atmosphere. Since the work in this thesis primarily focuses on characterization aspects, the synthesis will not be discussed further. Table 3.1 summarizes all samples investigated in this thesis. For simplicity, when referred to in this thesis, the samples are divided into four categories: "high", "intermediate", and "low" sodium content, with the Prussian blue sample being under "vacancies" since it contains no sodium, but has vacancies.

Table 3.1. *Overview of the samples investigated in this thesis. "Thesis sample name" are the names used in this thesis, while "paper sample name" are the samples' respective names in each paper.*

Thesis sample name	Composition	Paper sample name	Paper
High	$Na_{1.8(2)}Fe^{2+}_{0.78(7)}Fe^{3+}_{0.22(6)}[Fe^{2+}(CN)_6]\cdot 2.09(2)H_2O$	FS-PW	I
	$Na_{2.14(7)}Fe[Fe(CN)_6]\cdot 2.07(2)H_2O$	H-PW	II
	$Na_{2.08(7)}Fe[Fe(CN)_6]_{0.98(2)}$	D-PW	II
	$Na_{2.17(5)}Fe[Fe(CN)_6]\cdot 1.96(2)H_2O$	CP-PW	II
	$Na_{2.04(2)}Fe[Fe(CN)_6]\cdot 2.24(2)H_2O$	Hydrated PW	III
	$Na_{2.04(2)}Fe[Fe(CN)_6]$	Dehydrated PW	III
	$Na_{1.90(9)}Fe^{2+}_{0.90(7)}Fe^{3+}_{0.10(3)}[Fe^{2+}(CN)_6]\cdot 2.12(2)H_2O$	Na1.9	IV-V
	$Na_{2.05(5)}Fe[Fe(CN)_6]\cdot 2.07(2)H_2O$	Na2.0	V
Intermediate	$Na_{1.1(2)}Fe^{2+}_{0.39(6)}Fe^{3+}_{0.61(5)}[Fe^{2.3+}(CN)_6]\cdot 1.57(1)H_2O$	HS-PW	I
Low	$Fe[Fe(CN)_6]\cdot 0.807(9)H_2O$	DS-PW	I
	$Na_{0.34(5)}Fe^{3+}[Fe^{2.66(5)+}(CN)_6]\cdot 0.360(4)H_2O$	Na0.3	IV-V
Vacancies	$Fe[Fe(CN)_6]_{0.75}\cdot 1.5H_2O$	PB-1	I

3.2 Neutron scattering

A neutron is a neutral particle that is part of the atomic nucleus and has a mass and a magnetic moment. Thermal neutrons have an energy of around 25 meV corresponding to wavelengths of a few Å. This wavelength is on the same order of magnitude as interatomic distances in materials and can thus be used to probe the atomic structure. Neutrons can also be used to study excitations in materials because the neutron energy matches the energy change involved in various excitations, *e.g.,* phonons or crystal field excitations [23]. In neutron scattering experiments, the neutrons are treated as waves when interacting with a sample. A neutron is characterized as a plane wave with an initial wave vector $\mathbf{k_i}$ and energy $E_i = (\hbar^2 k_i^2/2m_n)$.[1] After scattering *via* a nuclear interaction with the sample, the wave vector changes to the final wave vector $\mathbf{k_f}$ and energy $E_f = (\hbar^2 k_f^2/2m_n)$ [23]. The measured quantity in a neutron scattering experiment is the differential cross section $\frac{d^2\sigma}{d\Omega dE_f}$ which is the number of scattered neutrons per time

[1] $\hbar$ is the reduced Planck's constant, m_n is the neutron mass, $d\Omega$ is solid angle subtended by the detector, and σ is scattering cross section.

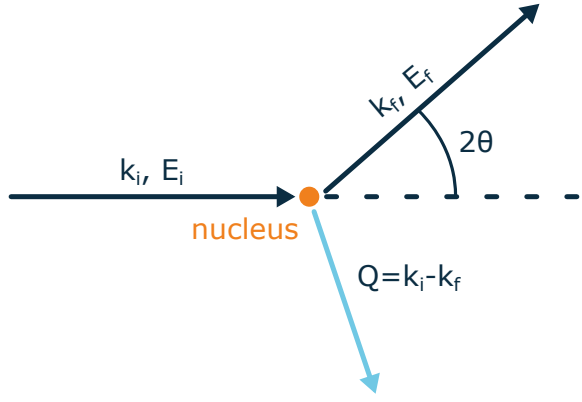

Figure 3.1. Scattering of neutrons by a nucleus with incident wave vector $\mathbf{k_i}$ and energy E_i and final wave vector $\mathbf{k_f}$ and energy E_f.

unit onto a small solid angle $d\Omega$ with final energy E_f. Because neutrons interact with the atomic nucleus, the point scatter approach works well for describing neutron scattering (Figure 3.1). The scattering data is expressed as a function of the momentum transfer $\hbar Q$ and energy E. The scattering vector $\mathbf{Q}$ (Equation 3.1) describes the relation between the incident ($\mathbf{k_i}$) and scattered beam ($\mathbf{k_f}$).

$$\boldsymbol{Q} = \boldsymbol{k_i} - \boldsymbol{k_f} \tag{3.1}$$

The magnitude of the scattering vector can be expressed in terms of the energy (Equation 3.2) [23].

$$Q^2 = \frac{2m_n}{\hbar^2}\left(E_i + E_f - 2\sqrt{(E_i E_f)}\, cos(2\theta)\right) \tag{3.2}$$

where 2θ is the angle between the incident and final neutron wave vectors. The accessible Q,E space depends on the incident energy and available scattering angles, and thus, varies between instruments. These parameters should therefore be carefully selected when designing the experiment. The scattering process is called elastic when there is no change in the neutron's energy after interacting with the sample. Thus, only a change in the momentum is detected. The process is called inelastic scattering if there is a change in the neutron energy after interacting with the sample. Here, a change in momentum and energy is detected.

The scattering cross section above does not take into account the different scattering amplitudes of the same element. Each isotope of an element has its own scattering length b. In addition, if the isotope has a spin, the isotope will have two scattering lengths b_+ and b_- [23]. This is because the scattering power depends on the spin of the neutron relative to the spin of the nucleus. The spin of the nucleus can randomly flip, generating the two observed scattering lengths b_+ and b_- when interacting with the neutron's

spin. Taking the isotope and spin effects into account (for several elements in a material), the scattering cross section consists of both coherent and incoherent scattering (Equation 3.3).

$$\frac{d^2\sigma}{d\Omega dE_f} = \left(\frac{d^2\sigma}{d\Omega dE_f}\right)_{coh} + \left(\frac{d^2\sigma}{d\Omega dE_f}\right)_{incoh} \tag{3.3}$$

Coherent scattering gives information about collective behavior, *i.e.,* self-other correlations. Incoherent scattering lacks coherence in scattering between the nuclei, and thus, the scattering amplitudes of the nuclei can vary in time and space. Incoherent scattering provides information about individual atoms regardless of their arrangement relative to other atoms, *i.e.,* self-self correlations.

In summary, neutron scattering provides information about the atomic structure and dynamics in many materials since both Q and E are measured giving a wide range of length ($l \sim \frac{1}{Q}$) and time ($t \sim \frac{1}{E}$) scales.

3.2.1 Neutron diffraction

Neutron diffraction is a coherent elastic method probing the atomic structure of materials. This method is the main technique used in this thesis to determine the structures of iron-based PBAs. With neutron diffraction, it is possible to distinguish between carbon and nitrogen (b_{coh} = 6.6 fermi for C and b_{coh} = 9.4 fermi for N)[2], which are almost impossible to detect with X-rays due to their low and similar scattering lengths (6 and 7 electrons for C and N, respectively), especially in the presence of the strongly scattering iron (26 electrons). Additionally, it is expected to be possible to differentiate a sodium ion (Na^+) and a water molecule (10 electrons each) using neutrons (b_{coh} = 3.6 fermi for Na, b_{coh} = 5.8 fermi for O, and b_{coh} = -3.7 fermi for H). However, X-ray diffraction provides complementary information and should not be neglected.

Powder diffraction

Powder diffraction is a useful technique to study the average structure of crystalline materials. In a powder diffraction experiment, a powdered sample is irradiated by *e.g.,* X-rays or neutrons, and the diffracted radiation is detected and analyzed. Typically, a powder consists of multiple randomly oriented small crystallites, where the individual crystallites consist of repeating units in space (called the unit cell) containing all the information needed to generate the crystal. Due to the long-range periodicity in the crystal, stemming from the unit cell and space group symmetry elements, the scattered waves will interact constructively (or destructively). The coherent scattering of radiation from the crystallites results in a diffraction

[2] 1 fermi = 10^{-15} m

pattern that is a fingerprint of the specific crystal structure observed with diffraction. Bragg's law describes the relationship between the radiation wavelength λ, the inter-planar spacing d_{hkl}, and the scattering angle θ (Equation 3.4) [24].[3]

$$n\lambda = 2d_{hkl}sin(\theta) \tag{3.4}$$

where n is an integer ≥ 1. The Miller indices (hkl) describe the reciprocal intercept on the unit cell vectors and are used to index the different crystallographic planes in the crystal structure that are separated by inter-planar distances d_{hkl}. Note that in Equation 3.4, the scattering angle is given by θ, while an experimental diffraction pattern commonly is plotted as the scattered intensity as a function of the scattering angle 2θ. Using Bragg's law and the measured scattering angles, the inter-planar spacings for each hkl can be calculated and used to determine the unit cell size and space group symmetry. However, Bragg's law does not take into account the different atoms and their occupancies, positions, and displacements on the different crystallographic planes, *i.e.,* it does not contain any structural information. Therefore, one needs to consider the structure factor F_{hkl} (Equation 3.5), which is related to the intensity distribution of the measured diffraction pattern I_{hkl} (Equation 3.6) [23, 24].

$$F_{hkl} = \sum_{i=1}^{unit\ cell} b_i\ e^{-B_i \frac{sin^2\theta}{\lambda^2}}\ e^{2\pi i(hx_i+ky_i+lz_i)} \tag{3.5}$$

$$I_{hkl} \propto |F_{hkl}|^2 \tag{3.6}$$

where x_i, y_i, and z_i are the fractional coordinates of atom i in the unit cell, B_i is the atomic displacement factor describing the thermal vibrations of the atom i, and b_i is the coherent neutron scattering length for atom i [23]. For X-rays, b in Equation 3.5 is replaced with the atomic form factor f.

Structural information from a diffraction pattern can be obtained by evaluating the intensity, position, and peak shape of the Bragg reflections. As seen in Equation 3.5, the intensity depends on which atoms are present in the sample, the position of the atoms on the different crystallographic planes, and the atomic displacement factor, which describes the average displacement of the atom from its equilibrium position. A way to quantify this information is to use the Rietveld method [25]. In this method, a diffraction pattern is calculated using a starting structure and then compared against the observed data. The starting structure gradually changes by refining different structural parameters to improve the fit between the calculated and observed data until a satisfactory fit and a chemically reasonable refined structure are obtained. The square sum of the difference between the observed y_{obs} and the calculated y_{calc} intensities at the i^{th} step

[3] Here θ is defined as $\theta = \frac{2\theta}{2}$

of the pattern is minimized using a least-squares method (Equation 3.7).

$$\sum_i \left(w_i (y_{obs,i} - y_{calc,i})^2 \right) \rightarrow min \tag{3.7}$$

where w_i is the weight assigned to each intensity step with the sum running over all data points. The calculated intensities consist of different functions (Equation 3.8) that account for different effects such as the background intensity $y_{b,i}$, the scale factor S that is proportional to the volume fraction of the contributing phase(s) ϕ, the multiplicity factor j of the k^{th} reflection, the Lorentz factor Lp, preferred orientation O_k, the structure factor F_k, and the peak profile function Ω_{ik} which accounts both for instrument and possible sample effects [24].

$$y_{calc,i} = y_{b,i} + \sum_{\phi=1}^{phases} S_\phi \sum_{k=k_1}^{k_2} j_{\phi k} \cdot Lp_{\phi k} \cdot O_{\phi k} \cdot |F_{\phi k}|^2 \cdot \Omega_{i\phi k} \tag{3.8}$$

The first sum is over all contributing crystalline phases, while the second sum is over all calculated Bragg reflections of a specific phase. The peak shape is usually modeled using a Gaussian or Lorentzian function, or with the pseudo-Voigt function, which is a linear combination of a Gaussian and a Lorentzian function. The background in a diffraction pattern comes from the sample environment, diffuse scattering, absorption, and multiple or incoherent scattering. This is typically modeled using a polynomial or by linear interpolation, which is the case for the refinements in this thesis.

Rietveld refinements are evaluated by different agreement factors that determine how well the calculated model fits the observed data [26]. However, it is important to keep the chemistry of the material in mind when evaluating the fits. The Rietveld method relies on the search for a minimum (Equation 3.7) and every minima found is a possible solution to the fit. However, a low agreement factor in itself does not equal a good solution. Therefore, each solution has to be evaluated so that the solution makes chemical sense, *i.e.,* the refined parameters, such as site occupancies and bond lengths, must be reasonable.

The diffraction data presented in this thesis were collected using multiple different instruments both in-house and at large-scale facilities. The in-house X-ray diffraction data were collected on a Bruker D8 Advance diffractometer or on a STOE Stadi P diffractometer. The synchrotron X-ray data were collected at the P02.1 beamline at the German Electron Synchrotron (DESY) in Germany [27] or at the DanMAX beamline at the MaxIV Laboratory in Sweden. The neutron diffraction data were collected on the time-of-flight diffractometer POLARIS at the ISIS Pulsed Neutron and Muon Source in the United Kingdom [28] or on the time-of-flight diffractometer NOMAD at the Spallation Neutron Source in the USA [29]. Refinements of the data were done using TOPAS Academic V6 [30] and crystal structures were visualized in CrystalMaker [31].

Total scattering with pair distribution function analysis

Total scattering is an extended case of diffraction where both the Bragg and the diffuse scattering are considered. The Bragg scattering pattern consists of well-defined peaks arising from constructive interference effects from having atoms in a sample arranged in a periodic pattern. Diffuse scattering covers the scattering due to deviations from the average periodic structure, *i.e.,* the interference effects from any other atomic arrangements in the sample, and gives information about the short-range structure of a sample [32].

Total scattering data is converted into a function in real space called the pair distribution function (PDF). Before doing so, the data need to be corrected for contributions from other scattering processes, *e.g.,* inelastic scattering, scattering from the sample holder, *etc.*, to isolate the coherent elastic scattering signal originating from the sample only. The corrected scattering data is normalized to the numbers of scatters N and their scattering lengths b giving the total scattering structure function $F(Q)$. The PDF is obtained by Fourier transforming $F(Q)$ (Equation 3.9).

$$G(r) = \frac{1}{(2\pi)^3 \rho_0} \int_{Qmin}^{Qmax} 4\pi Q^2 F(Q) \frac{sin(Qr)}{Qr} dQ \tag{3.9}$$

where ρ_0 is the average atom number density in atoms per Å^3 [33]. The PDF is a histogram of interatomic distances in a material and shows the probability of finding an atom at a distance r from another atom in real space. This is expressed in the partial radial distribution function (RDF) $g_{ij}(r)$ (Equation 3.10).

$$g_{ij}(r) = \frac{n_{ij}(r)}{4\pi r^2 dr \rho_j} \tag{3.10}$$

where $n_{ij}(r)$ is the number of particles of type j at a distance between r and $r + dr$ from a particle of type i. ρ_j is the number density for particles j [33]. The sum of the RDFs add up to give $G(r)$ by weighting with their coherent scattering lengths (b_i, b_j) and concentrations (c_i, c_j) (Equation 3.11) [33].

$$G(r) = \sum_{i,j=1}^{n} c_i c_j b_i b_j (g_{ij}(r) - 1) \tag{3.11}$$

As seen in Equation 3.9, the Fourier transform is taken from a minimum to a maximum Q value since it is not possible to integrate from zero to infinity from an experimental point of view. High Q_{max} values are desired for total scattering experiments to obtain high resolution in real space. This can be achieved by using high energy X-rays or at spallation neutron sources, giving Q_{max} values up to 50 Å^{-1}. However, by extending the Q range, the inclusion of noise in the data also increases. Thus, determining the Q_{max} value is a trade-off between resolution in real space and noise level [32].

The total scattering data presented in this thesis were collected on the time-of-flight diffractometer NOMAD at the Spallation Neutron Source in the USA [29] and analyzed using small-box modeling in PDFgui [34] or big-box modeling in RMCProfile [35, 36].

3.2.2 Neutron spectroscopy

Neutron spectroscopy was applied to determine vibrational, translational, and rotational dynamics in iron-based PBAs. These dynamics are related to self-self correlations, and thus, scatter neutrons incoherently. Due to the large incoherent scattering cross section of hydrogen (82.0 barns)[4] [23, 37], the scattering from the water in the investigated samples will dominate, and thus, the coherent term in Equation 3.3 can be neglected.

Inelastic neutron scattering

Inelastic scattering is, as previously mentioned, when there is a change in the energy of the neutron after interacting with the sample. The neutron can both gain or lose energy when interacting with the sample (Figure 3.2). However, at very low temperatures, at which inelastic neutron scattering (INS) measurements are typically done, there is very little scattering with neutron energy gain [23]. This is because the neutron has to interact with an excitation from the sample to gain energy, and at low temperatures, there are very few sample excitations. Thus, only neutron energy loss is observed in INS spectra at very low temperatures. INS is often used as vibrational spectroscopy to study molecular vibrations in many materials. The technique is complementary to infrared and Raman spectroscopy but differs in the fact that there are no optical selection rules [23, 37]. This means that all modes in principle are possible to measure, however, the relative intensity strongly depends on the neutron scattering cross section of the atoms in the material. The intensities of the peaks are proportional to the amount of the atoms in the sample, their vibrational amplitudes (displacement), and their scattering cross section [37], and thus, the obtained INS spectrum is a direct measure of the vibrational frequency and amplitude of the nucleus of an atom in a sample [23]. For example, hydrogen has a large incoherent neutron scattering cross section and is also a very light element (it displaces easily), thereby having a huge contribution to the INS peak intensity.

The inelastic neutron scattering data presented in this thesis were collected on three different spectrometers covering different energy ranges and resolutions. The instruments used were the indirect geometry time-of-flight spectrometer TOSCA, covering the low frequency region, and the direct geometry time-of-flight spectrometer MAPS, covering the high frequency region, at the ISIS Pulsed Neutron and Muon Source in the United Kingdom

[4] 1 barn = 10^{-28} m^2

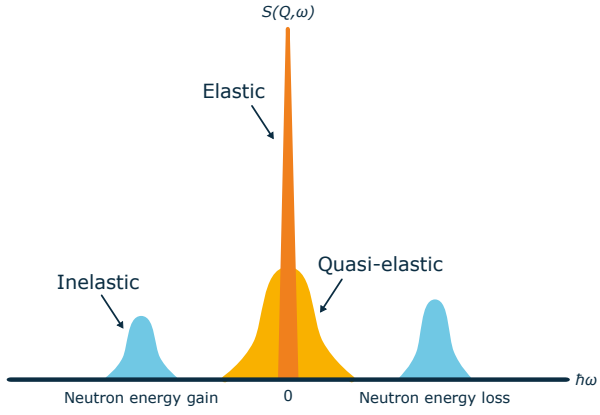

Figure 3.2. Elastic, quasi-elastic, and inelastic scattering regions.

[38–40]. In addition, INS data were collected on the indirect geometry time-of-flight spectrometer VISION at the Spallation Neutron Source in the USA [41]. VISION offers the possibility of measuring diffraction data simultaneously to probe the structure of the sample under investigation. This is especially useful for iron-based PBAs that exhibit many phase transitions as a function of the temperature. The data were analyzed through either lattice dynamics or molecular dynamics calculations based on density functional theory or ab initio molecular dynamics, respectively. The density functional theory calculated phonon results and the ab initio molecular dynamics trajectories were converted to calculated INS spectra using OCLIMAX [42, 43].

Quasi-elastic neutron scattering

Quasi-elastic neutron scattering (QENS) is a limited case of INS since there is a change in the neutron's energy after interacting with the sample, but the energy change is much smaller (μeV to a few meV) compared to the energy used for many excitations. The small energy change is caused by the interaction between the neutrons and atoms in the sample performing translations and/or rotational dynamics. Because these single-particle motions are not quantized, there is a continuous distribution of energies which gives rise to a broadening of the elastic line (Figure 3.2) [23]. The measured quantity in a QENS experiment is the incoherent scattering law $S(Q,\omega)$ [23].

$$S(Q,\omega) \sim R(Q,\omega) \otimes \left[\delta(\omega) A_E(Q) + \sum L_i(\omega) A_{QE,i}(Q)\right] \tag{3.12}$$

where ω is the angular frequency of the neutrons,[5] δ is a delta function used to describe the elastic scattering with area A_E, and L_i are the Lorentzian functions used to describe the quasi-elastic scattering with areas $A_{QE,i}$. From analysis of the QENS data, it is possible to separate long-range and localized

[5] $E = \hbar\omega$

dynamics. Long-range diffusion is characterized by the movement of the mass of a particle with the diffusing particle not being restricted in its movement within the structure. Localized dynamics (or restricted diffusion) are characterized by no mass transport of the diffusing particle. Thus, what is observed is the random rotation or change of orientation of a molecule in time where the mass is fixed in space [23].

Another phenomenon that can be observed with QENS is quantum rotational tunneling. Here, molecular groups are at low temperatures frozen into well-defined positions. This means that for the molecular group to undergo a rotation, it happens *via* tunneling through the energy barrier rather than going over the energy barrier. Tunneling is observed as satellite peaks centered around the elastic peak. These satellite peaks will slowly move closer to the elastic peak with increasing temperature until they become part of the quasi-elastic broadening [44]. Usually, tunneling happens at μeV energies meaning that the rotational barrier is quite high, however, as will be shown later in this thesis, tunneling can also occur at higher energies.

The quasi-elastic neutron scattering data presented in this thesis were collected on the cold neutron direct geometry time-of-flight spectrometer FOCUS at SINQ in Switzerland [45] and analyzed using DAVE [46].

3.3 Other characterization techniques

Inductively coupled plasma-optical emission spectroscopy

Inductively coupled plasma-optical emission spectroscopy (ICP-OES) and elemental analysis were used to determine the composition of the samples by calculating the atomic ratios of Na:Fe, C:N, and C:Fe. This gives information about the sodium and $[Fe(CN)_6]^{n-}$ vacancy content, which are important inputs when developing accurate structural models, especially if the scattering properties of certain elements are either low or similar to each other. The ICP-OES measurements reported in this thesis were performed by the company Medac Ltd in the United Kingdom.

Thermogravimetric analysis

TGA measurements give information about mass losses during heat treatment. Depending on the mass loss temperature, one can infer how much of a particular species has been lost. However, it should be noted that the identity of the lost masses cannot be distinguished by TGA alone, but in combination with mass spectrometry. In this thesis, the observed mass losses are assumed to be water up to ~250 °C based on previous TGA mass spectrometry measurements [47]. Knowledge of the water content in PBAs gives indirect information about the $[Fe(CN)_6]^{n-}$ vacancy content since a high number of $[Fe(CN)_6]^{n-}$ vacancies increases the porosity, and thus, the number of bare metal sites to which water can bind. The different water losses can

be related to different water sites within the structure of PBAs. This can in turn be combined with *e.g.,* variable temperature diffraction studies to understand how the structure changes upon heating.

Mössbauer spectroscopy

^{57}Fe Mössbauer spectroscopy is a useful technique for studying iron-based materials because of the possibility to probe the local chemical environment around iron in a material, *i.e.,* the oxidation states, local coordination chemistry and geometry, and ratios of the different iron sites. The technique has become particularly important for the investigation of $[Fe(CN)_6]^{n-}$ vacancies in iron-based PBAs due to ambiguity in determining the true composition of PBAs from other characterization techniques when both transition metal sites are occupied by iron. Additionally, indirect information about the cation content in the material can be obtained based on the oxidation states of iron, *i.e.,* the ratio of Fe^{2+} and Fe^{3+}, which can be determined from the center shift *CS* and the magnitude of the quadrupole splitting $|QS|$ (assuming that no other charge compensating ions are present in the sample). The Mössbauer experiments and analysis reported in this work were performed by collaborators. Thus, only the results obtained from the measurements and not the method itself will be discussed in this thesis.

Scanning electron microscopy

Scanning electron microscopy was used to determine the particle size and morphology of the synthesized samples. Depending on the synthesis method, different particle sizes and morphologies were obtained, which subsequently influence the properties. The method can also reveal if there are any surface deposits that might originate from impurities in the sample or if particle cracking is present.

Positron annihilation lifetime spectroscopy

To obtain further insight into the internal porosity and hence the composition of PBAs, positron annihilation lifetime spectroscopy (PALS) was used. PALS is able to probe defects in a material and quantify them within a certain sensitivity range by measuring the lifetime of a positron inside a material. This can then be related to the water, sodium, and $[Fe(CN)_6]^{n-}$ vacancy content, which all influence the internal porosity in PBAs. The measurements were performed by collaborators. Thus, only the results obtained from the measurements and not the method itself will be discussed in this thesis.

4. Determining accurate compositions

The large compositional and structural space for iron-based PBAs (and PBAs in general) leads to a wealth of properties. The composition of iron-based PBAs is particularly challenging to determine since both transition metal sites are occupied by iron in $Na_{2-4y-x}Fe[Fe(CN)_6]_{1-y}\cdot zH_2O$ (with $0 \leq x \leq 2$ and $0 \leq y \leq 0.5$). To accurately determine the vacancy content (y) the two iron sites need to be distinguished from each other. The vacancy content is the key component of the composition to determine since both the water content (z) and the sodium content (x) are dependent on this. The first study (Paper I) was therefore dedicated to determining the internal porosity of iron-based PBAs using the PALS method for the first time. However, before applying a new method or any complex characterization tool, the composition of the samples needs to be established using current characterization methods.

By applying X-ray diffraction, Mössbauer spectroscopy, TGA, and ICP-OES, the composition and structure of the samples were determined (Table 4.1). The water content for all four samples was in line with similar compositions previously reported [47, 48]. From ICP-OES, problems regarding the sodium and vacancy content were found. For example, for the high sodium sample, a sodium content above 2 sodium ions per f.u. was found, which is unlikely since it would indicate that iron has an oxidation state lower than 2+. Sodium was also detected in the sample with vacancies, which is unexpected when considering the non-reducing synthesis conditions. This

Table 4.1. *Composition and structure of high, intermediate, low, and low sodium with vacancies samples as determined from X-ray diffraction, ICP-OES, Mössbauer spectroscopy, and TGA. The ICP-OES and Mössbauer results state the sodium content per f.u., while it is water molecules per f.u. for the TGA results.*

Sample	TGA *z*	ICP-OES *x*	X-ray diffraction *symmetry*	Mössbauer *x*	Mössbauer *1-y*
High	2.09(2)	2.34(6)	$R\bar{3}$	1.8(2)	0
Intermediate	1.57(1)	1.52(5)	$Fm\bar{3}m$	1.1(2)	0
Low	0.807(9)	0.19(3)	$Fm\bar{3}m$	0	0
Vacancies	1.5	0.30(2)	$Fm\bar{3}m$	0	0.75

implies that the samples contain a sodium impurity. For all three samples without vacancies, the C:Fe ratio was found to be more than 3, suggesting that the impurity could contain carbon and/or nitrogen in addition to sodium. If the impurity is crystalline and there is a substantial amount present in the sample, it can be observed in the X-ray diffraction pattern. However, all four samples were phase pure with phases that are expected for the different sodium contents, except for the sample with an intermediate sodium content. Here, a $Fm\bar{3}m$ phase was determined. The sodium content of 1.52(5) per f.u. determined from ICP-OES does not match the $Fm\bar{3}m$ symmetry determined from X-ray diffraction since a sodium content of 1.52(5) per f.u. lies in the compositional range where a two-phase mixture is expected [11]. Thus, the X-ray diffraction results suggest that this sample also contains less sodium than determined from ICP-OES, as seen for the other samples.

Due to the ambiguity regarding the sample compositions, especially from ICP-OES, Mössbauer spectroscopy was applied. That is, the sodium content can be determined by evaluating the valence sum of the two iron sites. For all four samples, the sodium content was found to be lower than what was determined from ICP-OES. The vacancy content was determined to be zero for the high, intermediate, and low sodium samples, while the vacancy-rich sample had 25% $[Fe(CN)_6]^{4-}$ vacancies as expected from the synthesis. The final compositions determined after careful characterization were $Na_{1.8(2)}Fe[Fe(CN)_6]\cdot 2.09(2)H_2O$ (high), $Na_{1.1(2)}Fe[Fe(CN)_6]\cdot 1.57(1)H_2O$ (intermediate), $Fe[Fe(CN)_6]\cdot 0.807(9)H_2O$ (low), and $Fe[Fe(CN)_6]_{0.75}\cdot 1.5H_2O$ (vacancies). Since all four samples have additional sodium detected by ICP-OES, this raises a question as to whether the extra sodium comes from the sample preparation for ICP-OES analysis. Thus, elemental composition can not be supported by ICP-OES alone, but should include a combination of techniques.

4.1 Positron annihilation lifetime spectroscopy

From the combination of characterization techniques discussed above, the compositions of the four PBA samples were determined with well-quantified sodium, water, and/or $[Fe(CN)_6]^{n-}$ vacancy contents. PALS probes the electron density by evaluating the lifetime of a positron within a material. Thus, the PALS results can reliably be related to the internal porosity of the four samples through cross comparison with compositional and structural data.

Firstly, the average lifetime was evaluated. The average lifetime of the positron increases from 337(3) ps to 397(3) ps with decreasing sodium and water content (Figure 4.1a). Furthermore, when the $[Fe(CN)_6]^{n-}$ vacancy content increases, the average lifetime increases to 423(5) ps as seen for the sample with vacancies. Typically, a change in the average lifetime of 2 ps

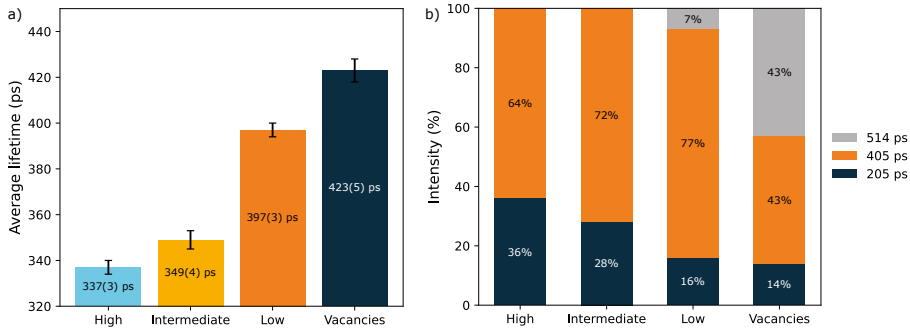

Figure 4.1. a) Average positron lifetime for the high, intermediate, low, and low sodium with vacancies samples. b) The lifetime components and their related intensity for each sample. For all four samples, two lifetimes (205 and 405 ps) were fixed in the fitting. For the low sodium sample and the sample with vacancies, a third component with a lifetime of ~514 ps was observed.

is considered a significant change [49] and implies a change in the cavities within the structure. Here, changes between 12 and 48 ps are observed throughout the investigated samples, illustrating a significant change in the average lifetime. When the sodium and water content decreases (with no significant changes in the unit cell volume), more space becomes available in the large cavities of the PBA framework. This leads to less electron density in the cavities, resulting in a longer average positron lifetime. When $[Fe(CN)_6]^{n-}$ vacancies are present, the internal porosity increases further, leading to a longer average lifetime. However, some of this space is occupied by water molecules, resulting in a shorter lifetime due to the increased electron density. Thus, the presence of water molecules counteracts the effect that $[Fe(CN)_6]^{n-}$ vacancies have on the average lifetime. Yet, the average lifetime is still higher for the sample with vacancies relative to the vacancy-free samples.

By evaluating the PALS spectra with a free fit (all parameters allowed to be refined), two positron lifetimes were found. A lifetime of 205 ps is present for all four samples, indicating a cavity in the structure that is similar. A second higher lifetime was determined, which increases from 369(1) ps to 458(2) ps with decreasing sodium content. For the sample with vacancies, the second lifetime is 471(1) ps. The two lifetimes were fixed at 205 ps and 405 ps in the fitting procedure to ensure comparable lifetime intensities between the samples (Figure 4.1b). The intensity gives the relative proportion of each type of defect that the positron experiences at a specific lifetime. For the 205 ps lifetime, the relative intensity increases when the sodium and water content increases, and the $[Fe(CN)_6]^{n-}$ vacancy content decreases. This can be explained by the smaller distance between sodium and water in the fully sodiated material giving a higher electron density within the structure

resulting in a shorter lifetime of the positron. For the 405 ps lifetime, the intensity decreases when the sodium and water content increases. This result shows that the fraction of positron annihilation events in this type of defect decreases when more sodium and water are present in the structure. For a high $[Fe(CN)_6]^{n-}$ vacancy content, the relative intensity of the 405 ps lifetime is lower than for the high sodium sample (43% *vs* 64%). Thus, this lifetime falls out of the trend that the other samples follow. It should be noted that a higher percentages of $[Fe(CN)_6]^{n-}$ vacancies increase the porosity relative to the vacancy-free samples, however, some of the porosity is lost since the vacancies are filled with water molecules. Additionally, a third high-intensity component with a lifetime of ~514 ps was observed for the sample with vacancies indicating another dominant positron trap within the structure of Prussian blue. The third component could stem from a surface effect due to the smaller particle size for this sample. The presence of the third component makes it hard to compare the relative intensities of the sample containing vacancies with the vacancy-free samples. Despite that, the 205 ps lifetime was observed for all four samples indicating a positron trap that is the same in all four samples independent of the sodium, water, and/or $[Fe(CN)_6]^{n-}$ vacancy content. Taking the relative intensity ratio of the 405 ps and 205 ps as a function of the water content (Figure 4.2), it is clear that the observed lifetimes are mostly correlated with the water content.

In summary, the PALS method showed a correlation between the average positron lifetime and the degree of filling of the cavities in the structure of iron-based PBAs. Despite that, the method does not give insight into how this is related to the successive filling of the cavities by sodium and water and/or the presence of $[Fe(CN)_6]^{n-}$ vacancies in varying concentrations.

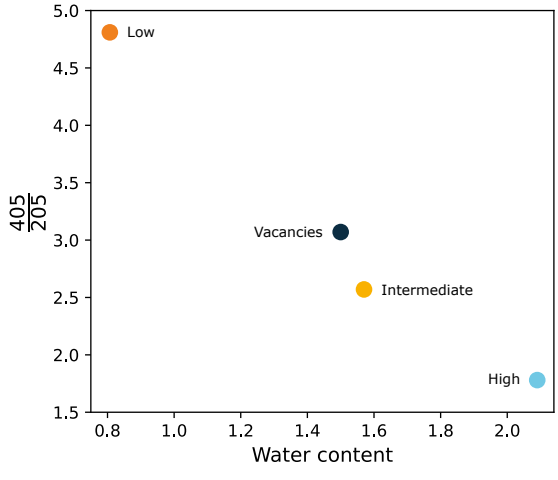

Figure 4.2. Relative ratios of the 405 ps and 205 ps lifetime intensities as a function of the water content.

Nevertheless, since the average lifetime changes significantly between the samples, there is a large compositional space of PBAs that can be examined in future studies. To improve the PALS method as a characterization tool for PBAs, further investigation is needed. For example, the accuracy of the PALS method compared to the other standard methods (ICP-OES, Mössbauer spectroscopy, TGA, and X-ray diffraction) needs to be determined as well as how the presence of impurities affects the PALS results. In addition, knowledge about which cavity each lifetime corresponds to within the structure is needed, which can be aided by computational modeling. This work shows that a combination of these characterization methods is crucial to unravel the true composition of iron-based PBAs and further proves that Mössbauer spectroscopy is a powerful method to obtain reliable and complementary information to the other characterization techniques.

5. Temperature and composition dependent phase transitions

Paper II presents the first neutron diffraction study of iron-based PBAs with a high sodium and low vacancy content ($Na_2Fe[Fe(CN)_6]\cdot zH_2O$, Table 3.1 Paper II). The compositions and phase purity of the studied samples were determined using ICP-OES, Mössbauer spectroscopy, TGA, and X-ray diffraction. The focus was to determine accurate atomic structures of the hydrated and dehydrated phases and to follow the structural changes between these phases from room temperature (~298 K) to 523 K. In the literature, there is not yet a consensus about the structure, especially for the hydrated material, due to the extensive use of X-ray diffraction alone to study the structure. Neutron diffraction provides a solution to this since it is possible to differentiate between carbon and nitrogen, and also between a sodium ion and a water molecule. To investigate the impact of the synthesis method, the structure of a sample made by a co-precipitation synthesis method was compared to that of a sample produced by the acid decomposition synthesis method. The refined structures were differentiated in terms of their octahedral tilt system and sodium displacement. This is a useful way of interpreting PBA structures since PBAs tend to distort when the $[M'(CN)_6]^{n-}$ vacancy content is low and the alkali cation content is high, which is the case for most of the investigated PBAs in this thesis [11].

5.1 The average structure of the hydrated material

Variable temperature neutron diffraction was carried out on the hydrated sample synthesized using acid decomposition and revealed a near room temperature phase transition (Figure 5.1a). The room temperature pattern consists of two phases with $P2_1/n$ and $R\bar{3}$ symmetry due to an incomplete phase transition between 303 and 313 K (30-40 °C). The $R\bar{3}$ phase is visible in the room temperature diffraction pattern at 2.6 Å by the presence of the $20\bar{4}$ reflection of the $R\bar{3}$ phase between the 022 and 400 reflections of the $P2_1/n$ phase. The phase transition is complete at 313 K. Interestingly, this phase transition is also observed for the hydrated sample with a similar composition but synthesized via a co-precipitation synthesis method (Figure 5.1b) indicating that the phase transition is independent of the synthesis method. Thus, unlike previously reported [50], the structure of the material depends

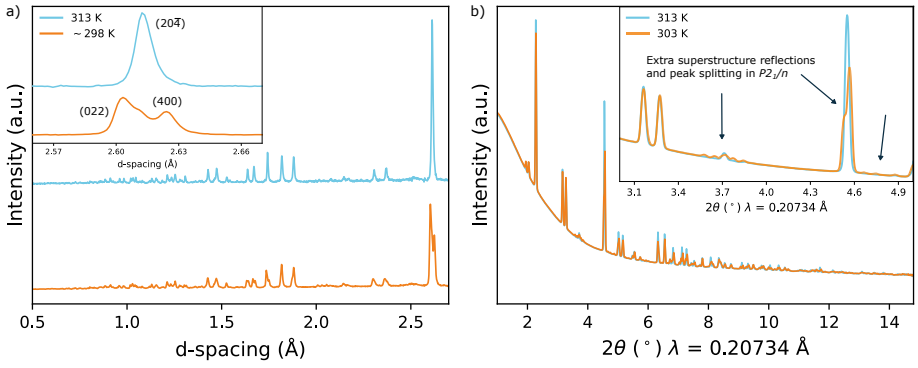

Figure 5.1. a) Neutron diffraction data of the hydrated sample synthesized using acid decomposition. The inset shows the split peak at 2.6 Å in the room temperature data. b) Synchrotron X-ray diffraction data of the hydrated sample synthesized using co-precipitation. The inset shows the main difference between the $P2_1/n$ and $R\bar{3}$ phases, which are the extra superstructure reflections at 3.5-3.6° and 4.7° and peak splitting at 4.5° in the $P2_1/n$ pattern.

on the composition rather than the synthesis method. The $P2_1/n$ and $R\bar{3}$ structures have previously only been reported individually at room temperature [19, 50, 51]. The data presented in this thesis is the first to show that both symmetries can exist for the same composition, separated by a phase transition close to room temperature.

The phase transition from $P2_1/n$ to $R\bar{3}$ can be explained in terms of octahedral tilting, which is common for PBAs, and influences the material properties [11, 52]. Typically, PBAs with a high sodium or potassium content have the tilt pattern $a^-a^-b^+$ driving the monoclinic $P2_1/n$ symmetry (Figure 5.2a). This means that one of the crystallographic axes has an in-phase tilt (+) along the pseudo-cubic axis with a specific magnitude (b), while the two other directions have an out-of-phase tilt (-) with another magnitude (a) [53]. Dehydrated sodium-containing PBAs often have the tilt pattern $a^-a^-a^-$ driving the $R\bar{3}$ symmetry (Figure 5.2b). Here, all three crystallographic axes exhibit an out-of-phase tilt with the same magnitude. The two tilt patterns are differentiated in the room temperature diffraction pattern by the appearance of the split peak at 2.6 Å indicating that one of the three crystallographic axes is different from the other two (Figure 5.1a).

Since the room temperature diffraction pattern of the hydrated sample (synthesized using acid decomposition) has two phases present, the diffraction pattern at 313 K was refined first using symmetry-mode refinements with space group $R\bar{3}$. With the final structural model for the $R\bar{3}$ phase established, it could be included as the second phase with fixed parameters in the refinement of the room temperature diffraction pattern using $P2_1/n$ symmetry. The phase fractions were determined to be 82.8(5)% and 17.2(5)% for the $P2_1/n$ and $R\bar{3}$ phases, respectively. For both models, hydrogen was

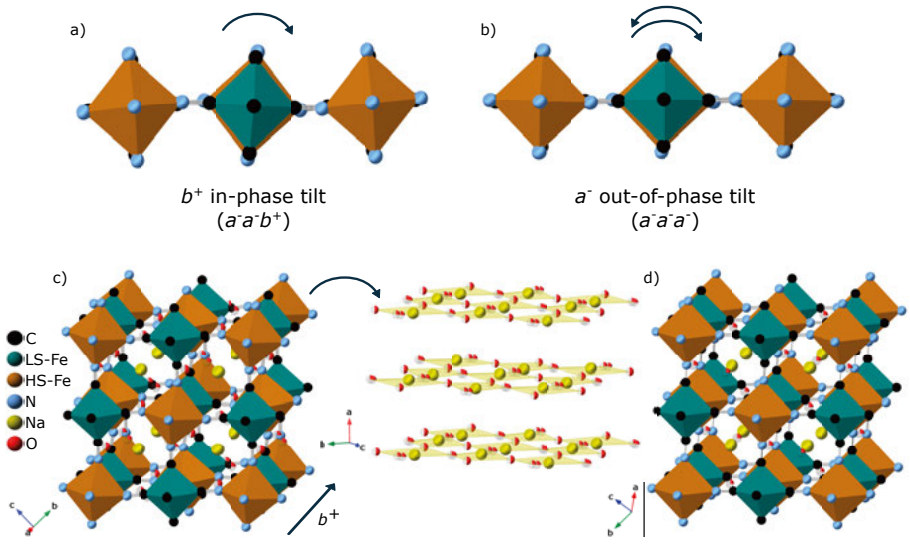

Figure 5.2. The tilt patterns for the a) monoclinic $P2_1/n$ and b) rhombohedral $R\bar{3}$ symmetries. c) Pseudo-cubic structural representation emphasizing the sodium channels along the *a* direction and the layering of sodium and oxygen in the *bc*-plane in the $P2_1/n$ model. d) Pseudo-cubic structural representation of the $R\bar{3}$ model.

not included due to the positional and orientational disorder of the water molecules.

In the room temperature $P2_1/n$ structure (Figure 5.2c), the oxygen atoms are randomly distributed within the *bc*-plane, occupying four of the six window faces of each PBA subcube. This arrangement results in clear sodium channels along the *a* direction. Notably, these channels are along the same direction as the in-phase tilt (b^+), suggesting that the position of water might direct the nature of the tilting in PBAs. One of the oxygen atoms was included as a split site in the $P2_1/n$ model, indicating that water in fact must lie slightly closer to one of the sodium atoms. However, these displacements are not long-range ordered and thus give rise to a split site in the model of the average structure. The final $R\bar{3}$ structure at 313 K (Figure 5.2d) has oxygen distributed on three of the window faces of each subcube with no clear sodium channels. For the 313 K data, it was found that several different models with different distributions of oxygen atoms could fit the data equally well. Consequently, the data suggest that the water is more disordered in the $R\bar{3}$ model than in the $P2_1/n$ model. To unravel the local order of water in the $R\bar{3}$ structure, neutron total scattering experiments are necessary and will be discussed in Chapter 6.

5.2 Dehydration mechanism

The structural evolution was studied by following the dehydration using variable temperature X-ray and neutron diffraction (Figure 5.3). Firstly, the hydrated material adopts a $P2_1/n$ phase, which converts to an $R\bar{3}$ phase close to ~308 K. Depending on the heating rate used (1 K/min for X-rays *vs* 0.4 K/min for neutrons), a phase transition to $Fm\bar{3}m$ happens at ~393 K and ~449 K, respectively. The $Fm\bar{3}m$ phase co-exists with a dehydrated $R\bar{3}$ phase from 493 to 518 K in the X-ray diffraction data. Notably, the transition to the $Fm\bar{3}m$ phase did not go to completion before conversion to the dehydrated $R\bar{3}$ phase at 503 K in the neutron diffraction data. The different sample sizes used in the X-ray and neutron experiments (~2 mg *vs* ~2 g) also affect the heating homogeneity and the rate of water removal through the whole sample. However, it is clear that the dehydration process heavily depends on the heating rate used [51]. Reasons for the limited kinetics can be explained by the strong interaction between sodium and water within the structure [47], the large diffusion pathways across the micron-sized particles, and the energy required to convert to the strained dehydrated $R\bar{3}$ phase.

To investigate the structural changes from dehydration, neutron diffraction data on a fully dehydrated sample were collected. The volume shrinks by 20% upon dehydration relative to the hydrated material, and the crystallinity is lowered as indicated by the broadening of the diffraction peaks (Figure 5.4a). However, it is important to note that the symmetry of the 313 K structure and the dehydrated structure is the same, both being $R\bar{3}$. Symmetry-mode refinements revealed the key distortion modes and the magnitude with which they change upon dehydration. The key distortion modes include displacement of sodium along the *c* direction towards the nitrogen-bound iron octahedra and tilting of the rigid iron octahedra (Figure 5.4b-c). The sodium displaces along *c* due to the Coulombic attraction to the electron-dense nitrogen-bound iron atoms. Simultaneously, the rigid iron octahedra are rotated with the Fe-C-N angle remaining unchanged due to the strong π-backbonding character of the Fe-C bond. The sodium dis-

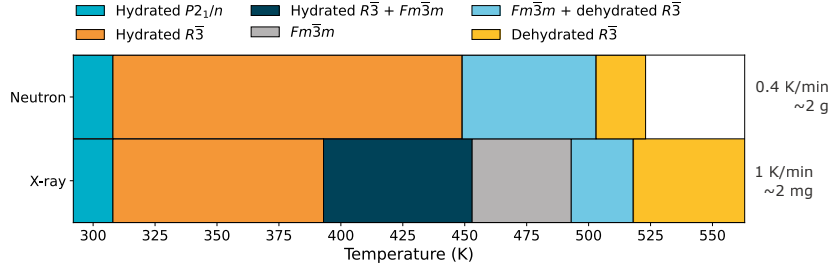

Figure 5.3. Variable temperature phase diagram extracted from the X-ray and neutron diffraction data for the hydrated material synthesized using acid decomposition.

placement is also evident from the refined distortion magnitudes (see details in Paper II). Here, the Γ_5^+ irrep responsible for sodium displacement increases from 0.05(1) to 1.358(4) Å reflecting the distance that sodium displaces toward the nitrogen-bound iron atom relative to its original position in the hydrated $R\bar{3}$ structure. The structural collapse can also be interpreted from the iron octahedra rotation angles that increase from 1.69(1)° to 17.44(6)° for the carbon-bound iron octahedra and 1.52(7)° to 22.60(4)° for the nitrogen-bound iron octahedra. Thus, removing water does not induce phase transitions but rather modifies the magnitude (a) of pre-existing distortions within the $R\bar{3}$ symmetry.

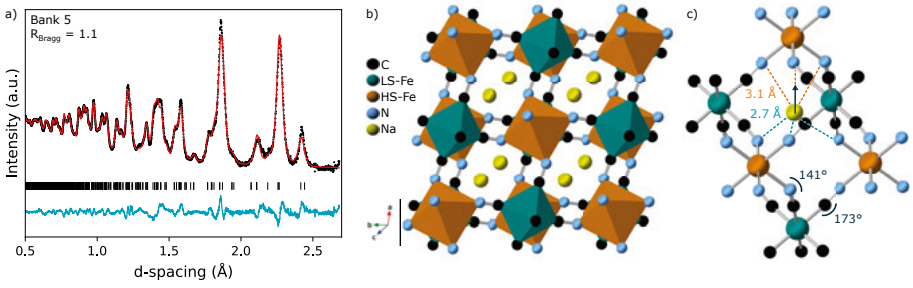

Figure 5.4. a) Rietveld fit to the neutron powder diffraction data of the dehydrated sample. The data are shown as black dots, the calculated pattern in red, and the difference curve in blue. Allowed reflections for $R\bar{3}$ are represented by black vertical lines. b) Pseudo-cubic structural representation of the dehydrated structure. c) Selected bond lengths and angles within a subcube. The arrow shows the direction in which sodium is displaced.

5.3 Thermal expansion

An interesting property arising from the large functionality of PBAs is negative thermal expansion. Therefore, the thermal expansion of the hydrated material was investigated from 313 to 413 K. Most PBAs have isotropic negative thermal expansion upon heating due to their cubic symmetry [12, 54–56]. However, the hydrated sample exhibits a small positive volumetric expansion and anisotropic thermal expansion with the *ab*-plane contracting and expansion along *c*. The coefficients of thermal expansion are α_{ab} = -1.2(9) $(MK)^{-1}$ and α_c = 34(2) $(MK)^{-1}$. When dehydrated, the material still exhibits anisotropic thermal expansion in the temperature range 303 to 523 K, however, with the *ab*-plane expanding and contraction along the *c* direction. The coefficients of thermal expansion are α_{ab} = 52.2(3) $(MK)^{-1}$ and α_c = -31.1(2) $(MK)^{-1}$. The dehydrated material also exhibits a positive volumetric expansion with increasing temperature, but with a higher rate of expansion compared to the hydrated material. This anisotropic thermal

expansion behavior is different compared to other PBAs due to the lower (non-cubic) symmetry, thereby making it hard to draw comparisons. Nevertheless, the different thermal expansion behavior of the hydrated and dehydrated materials suggests a strong influence of water and sodium on the magnitude and rate of thermal expansion. The fact that the direction of the thermal expansion changes when water is present indicates that water's interaction with the PBA framework is important to consider. Thus, local structural studies are necessary to unravel this behavior.

5.4 Phase transitions during battery cycling

The dehydrated material $Na_{2-x}Fe[Fe(CN)_6]$ is used as the positive electrode in sodium-ion batteries. As mentioned in Section 1.3, the material undergoes a phase transition from $R\bar{3}$ to $Fm\bar{3}m$ symmetry during charging, *i.e.,* sodium extraction. During discharge, *i.e.,* sodium insertion, the phase transition is, in principle, reversible. This phase transition involves large changes in the volume (±17%), which is considered detrimental to the material over time because of structural degradation and increased sodium ion insertion resistance [16]. In particular, a study showed that most of the capacity is lost from the lower voltage plateau where the phase transition occurs [57]. Paper VI presents a study of full cells consisting of the dehydrated material and hard carbon anodes, aiming to determine the structural evolution after prolonged cycling using different restricted potential ranges. These potential ranges were selected to isolate different regions where the phase transition occurs, *i.e.,* cycling only within the $Fm\bar{3}m$ solid solution, through the phase transition, or in between these two endpoints.

Based on the synchrotron *operando* X-ray diffraction data for all the cells, the possible degradation mechanisms were narrowed down to any combination of polarization, particle orphaning (both cracking and/or delamination), and/or sodium inventory loss, *i.e.,* inaccessible sodium for reversible reactions during cycling. Evidence for sodium inventory loss was found from the significant loss of the $R\bar{3}$ phase in the first couple of cycles. In addition, after prolonged cycling in different restricted potential ranges, which cycled the material only within the $Fm\bar{3}m$ solid solution range or partly through the phase transition, it was observed that the cells performed similarly and had more of the $R\bar{3}$ phase recovered when subsequently cycled in the full potential range (1.3-3.6 V) compared to cells cycled in the full potential range for many cycles. These results indicated that the structure might not be degraded from cycling through the phase transition, but that it is more likely that the $R\bar{3}$ phase is inaccessible because there is less sodium available in the system. More specifically, the phase transition depends on the composition, where the $R\bar{3}$ phase is obtained when the sodium content

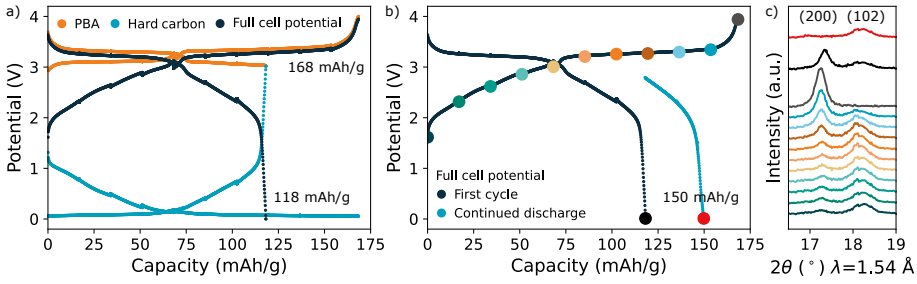

Figure 5.5. a) Electrochemical cycling of the 3-electrode cell consisting of a PBA electrode, a hard carbon counter electrode, and a sodium metal reference electrode. b) The cycling curve for the 3-electrode cell (dark blue) and the continued discharge curve (light blue) after sodiation of the hard carbon electrode. The colored dots correspond to the X-ray diffraction pattern in (c), showing the $Fm\bar{3}m$ 200 and $R\bar{3}$ 102 reflections, respectively.

is high, and is thus not possible to obtain when the sodium in the system is inaccessible.

To test the sodium inventory loss hypothesis, a 3-electrode cell consisting of a PBA working electrode, a hard carbon counter electrode, and a sodium metal reference electrode was built, and in-house *operando* X-ray diffraction was performed. Firstly, looking at the electrochemistry (Figure 5.5a), the hard carbon anode's potential rapidly increased upon discharge, while the PBA electrode was still on the lower voltage plateau when the full cell potential dropped to 1.3 V, giving a final capacity of 118 mAh/g. Secondly, the X-ray diffraction data showed the conversion to the $Fm\bar{3}m$ phase during charge (Figure 5.5b-c), however, at the end of discharge, a mixture of the two phases was present (51% $Fm\bar{3}m$ phase). The hard carbon counter electrode was then sodiated overnight, and the discharge was continued the day after resulting in a final discharge capacity of 150 mAh/g and 7% $Fm\bar{3}m$ phase present. Thus, by adding more sodium to the system, a higher percentage of the $R\bar{3}$ phase was obtained demonstrating that the structure has not completely degraded and that sodium can be inserted into the structure. The difference between the initial capacity of 168 mAh/g and the final capacity of 150 mAh/g could be due to side reactions, inactive materials, and/or polarization, as the lower voltage plateau for the PBA electrode had been passed. The polarization could be due to volume changes since the initial cracking caused by the phase transition can cause particle orphaning. In summary, by using the learnings from the fundamental studies of the composition and phase transitions (Papers I-II), it was possible to describe a property when the material is used in its desired application.

6. Beyond the average structure

Paper III presents the first neutron total scattering study of the local structure of iron-based PBAs with a high sodium content and low vacancy content ($Na_{2.04(2)}Fe[Fe(CN)_6]\cdot 2.24(2)H_2O$, Table 3.1 Paper III). The composition and phase purity of the studied samples were determined using ICP-OES, Mössbauer spectroscopy, TGA, and X-ray diffraction. In Chapter 5, disorder of the water was observed in the $P2_1/n$ phase as one of the oxygen atoms was included as a split site, while the ordering of the water was completely lost during the transition to the $R\bar{3}$ phase. Additionally, peak broadening in the diffraction pattern of the dehydrated material was observed, indicating a loss of crystallinity due to either strain or size effects. Because of these observations, there is a need for local structural insight. Neutron total scattering with PDF analysis can be used to obtain local and average structural information since both the Bragg and diffuse scattering are considered. The data were modeled using Reverse Monte Carlo (RMC), where the contents, *e.g.*, atoms or molecules, of a big box are moved around randomly until an agreement with the data is obtained. This method does not rely on symmetry, but the refinement can be driven by refining against different data, which contains different types of information about the system, and by applying constraints to obtain physically meaningful structures. This method is especially useful for modeling materials with disordered molecules, such as hydrated PBAs.

6.1 The neutron pair distribution functions

The neutron diffraction data of the high sodium hydrated material revealed that the $P2_1/n$ phase exists down to 100 K, with a transition to the $R\bar{3}$ phase between 300 and 330 K. The dehydrated material has $R\bar{3}$ symmetry at both 100 and 300 K. The neutron PDFs for the hydrated and dehydrated material show that below 5 Å, the peaks are sharper relative to the peaks at larger distances (Figure 6.1). This suggests that there is a structural unit that is well-defined, but that this structural unit arranges in a disordered way to make up the larger structure. Small-box modeling of the data from the dehydrated sample revealed that this structural unit corresponds to a PBA subcube with sodium (and water for the hydrated material) within the subcube. The arrangement of the subcubes to form the larger structure can affect the rigidity of the PBA framework. The distribution of sodium and water within the

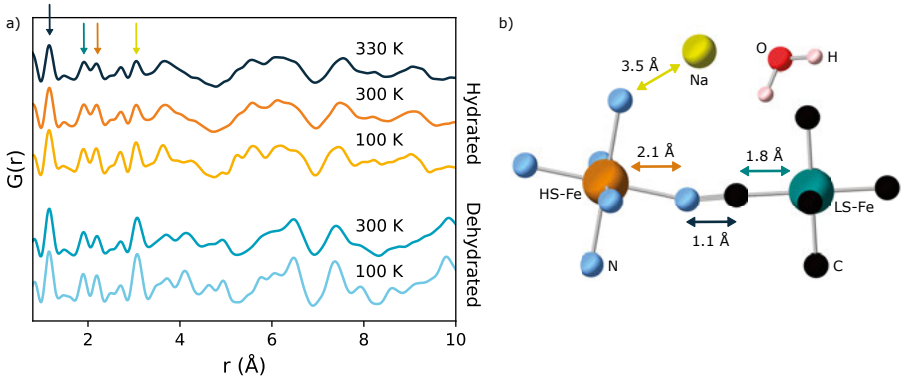

Figure 6.1. a) Neutron PDFs of the hydrated and dehydrated samples at 100 to 330 K. b) Selected pair distances present in the PDF.

framework can further create additional disorder. The main difference in the PDFs of the hydrated and dehydrated material is the presence of hydrogen in the hydrated sample, which makes the intensity of some peaks negative due to the negative coherent scattering length of hydrogen, *e.g.*, at 5 Å. The PDFs at 300 and 330 K for the hydrated material are visibly very similar, indicating only subtle differences in the local environment in the two phases. Thus, modeling of the data is needed to obtain accurate structural information from the PDFs.

6.2 The local structure of the hydrated material

The RDFs, describing the different atom pairs, were used to evaluate the PBA framework and the sodium and water coordination. The Fe-Fe RDF showed minor displacements of the iron atoms, indicating an ordered arrangement of iron throughout the larger structure. However, elongation of the Fe-N bonds and bond angle bending are present in the nitrogen-bound iron octahedra, while the carbon-bound iron octahedra remain rigid. The tilting of the PBA framework is very minor, with the Fe-C-N and Fe-N-C angles being centered around 180°, due to the presence of water that keeps the framework expanded.

The sodium RDFs reveal the coordination environment for sodium relative to the framework and itself. The Fe-Na/Na-Na RDFs show similar correlations at all distances, but with the Na-Na RDF being broader than the Fe-Na RDF, indicating that the sodium is more disordered throughout the structure than iron (Figure 6.2a). This is expected since the sodium has more degrees of freedom than iron, which is locked into the PBA framework. The cyanide ligands of the framework have more flexibility, and therefore, have different correlations to sodium than iron. The C-Na/N-Na RDFs con-

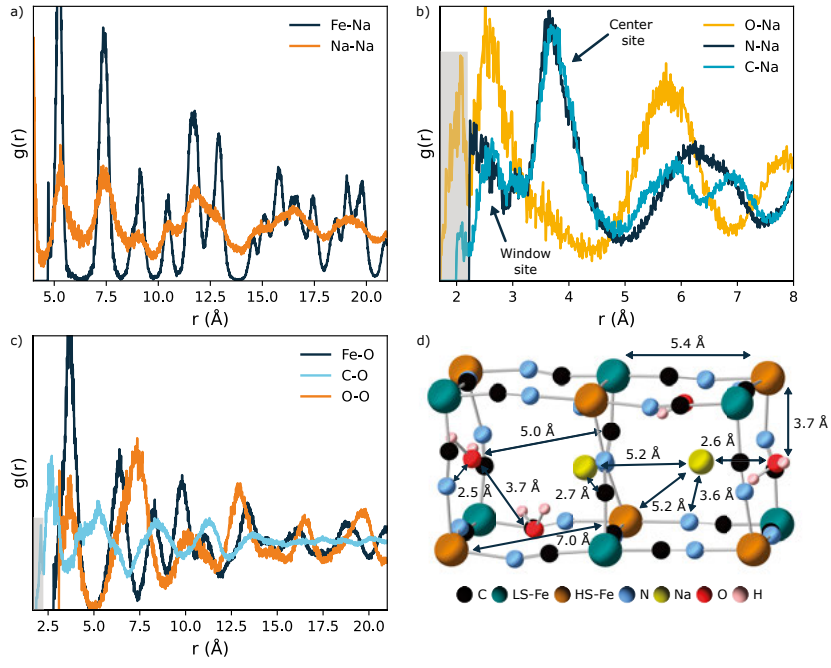

Figure 6.2. RDFs for the hydrated material. a) Fe-Na/Na-Na, b) O-Na/C-Na/N-Na, and c) Fe-O/C-O/O-O. d) Cutout of the RMC supercell showing the different local environments present. All data are shown for 300 K with similar observations at 100 and 330 K. The peaks in the grey shaded area are fitting artifacts due to the constraints applied in this region.

sist of three peaks up to 5 Å (Figure 6.2b). The peaks at 3.1 Å and 3.6 Å correspond to distances within a subcube (Figure 6.2d). These distances relate to sodium being positioned around the center of the subcube. A peak at 2.7 Å is also present in the RDF corresponding to sodium being closer to the window face. This is only observed if there is no water molecule on that window face. Thus, the majority of the sodium is found to be distributed around the center, while a small amount is closer to the cyanide ligands if no water molecule hinders its pathway. When entering a neighboring subcube (5-10 Å), the C-Na/N-Na RDFs deviate (Figure 6.2b). Sodium appears to be closer and more ordered relative to carbon, while there is a range of distances to nitrogen, indicating a more disordered correlation. This is due to the more disordered nitrogen that has a weaker bonding character and also stretches away from its associated iron. Above 7.5 Å, the C-Na/N-Na correlations become similar. This is observed in both the $P2_1/n$ and $R\bar{3}$ phases. The broad distribution of sodium is also evident in the condensed unit cells (Figure 6.3). In the $P2_1/n$ phase, the sodium is distributed in the *bc* plane, while it is less ordered but with distributions along preferred crystallographic directions throughout the framework in the $R\bar{3}$ phase. The ordering of sodium

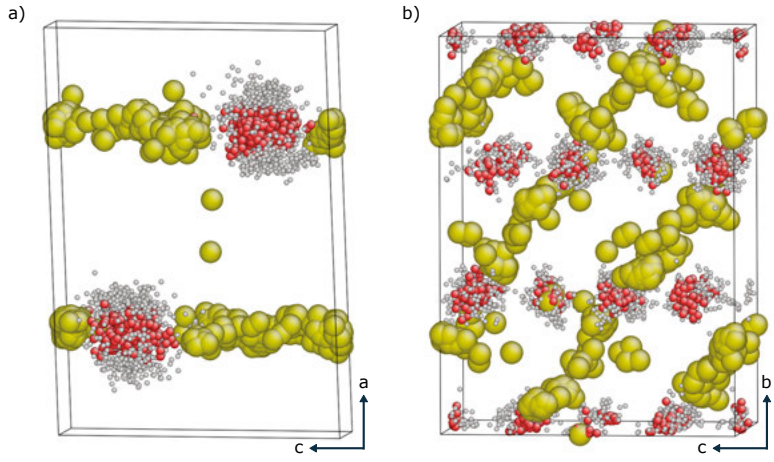

Figure 6.3. Condensed unit cells emphasizing the ordering of the sodium and water in a) the $P2_1/n$ phase at 300 K and b) the $R\bar{3}$ phase at 330 K. Sodium is shown in yellow, oxygen in red, and hydrogen in white.

into planes in the $P2_1/n$ phase might be due to the anisotropic tilt pattern $a^-a^-b^+$ (Chapter 5), making the channels along the b^+ direction different to the two other directions.

Since the sodium has a specific ordering (especially in the $P2_1/n$ phase), this might also affect the position and orientation of the water molecules. In the $P2_1/n$ phase, where sodium is in a plane, the water molecules are oriented with the oxygen in the same plane as sodium, while the hydrogen atoms point away from this sodium-oxygen layer (Figure 6.3a). In the $R\bar{3}$ phase, where sodium is less ordered, the water molecules also have less orientational order (Figure 6.3b). The sodium occupies a wide range of positions in the $R\bar{3}$ phase, which also drives the water to point in a wide range of directions since they are affecting each other due to increased mobility at this temperature. However, locally, the hydrogen atoms point away from the sodium, while the oxygen points towards the sodium. For both phases, the O-Na RDF has a distribution around 2.6 Å, indicating that sodium and water interact (Figure 6.2b). As will be shown later in Chapter 7, this distance is similar to the observed water cavity size from QENS. However, where this interaction is within the framework depends on the local position of sodium and water. The water also has a small distribution around its average position on the window face, which is reflected in the Fe-O/C-O RDFs (Figure 6.2c). The RDFs have distances in the 2.5-5 Å region corresponding to distances from iron and cyanide in the framework to the water molecule on the window face. The O-O RDF shows that the nearest neighboring water molecule is 3.7 Å away corresponding to two water molecules on adjacent subcube windows (Figure 6.2c-d). The medium-range ordering of the water molecules differs in the $P2_1/n$ and $R\bar{3}$ phases, which agrees with water occu-

pying more window faces in the $R\bar{3}$ phase than in the $P2_1/n$ phase. The Fe-O RDF has sharper peaks than the O-Na, C-O, and O-O RDFs, suggesting that the movement of the cyanide and water is more significant relative to that of iron and sodium (Figure 6.2b-c).

6.3 The local structure of the dehydrated material

The high sodium dehydrated sample also consists of a relatively ordered PBA framework, but with Fe-N bond elongation. This elongation is more severe than observed for the hydrated sample. The carbon-bound iron octahedra remain rigid. Since there is no water present, the iron octahedra tilt more. The Fe-N-C bond angle is more flexible due to the ionic character, resulting in a tilt angle distributed around 145°, while the more covalently-bound carbon results in an Fe-C-N bond angle distribution around 180°.

The diffraction pattern of the dehydrated sample exhibits peak broadening, which can be due to either a finite crystallite size or strain in the material. The sodium coordination environment shows that sodium is disordered relative to the framework. The Fe-Na/Na-Na RDFs both have their first peak at 4.0 Å (Figure 6.4a) corresponding to the distance between iron and sodium within one subcube, and the distance between two sodium atoms in neighboring subcubes (Figure 6.4c). The RDFs are not correlated

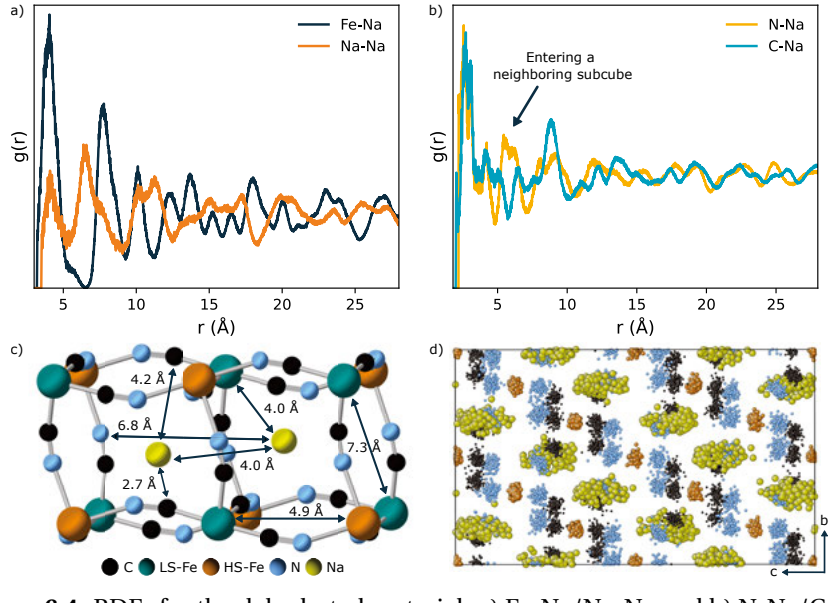

Figure 6.4. RDFs for the dehydrated material. a) Fe-Na/Na-Na and b) N-Na/C-Na. c) Cutout of the RMC supercell showing the different local environments present. d) Condensed unit cell emphasizing the distribution of sodium along *c*. All data are shown for 300 K with similar observations at 100 K.

at larger distances, and the Na-Na RDF is broader than the Fe-Na RDF, illustrating the disorder of the sodium throughout the framework. The sodium disorder combined with the Fe-N bond elongation contributes to the observed strain, *i.e.,* peak broadening, in the diffraction pattern. The sodium mainly shifts towards the cyanide ligands, especially the electron-dense nitrogen, for optimal bonding conditions, creating the two observed peaks at 2.7 and 3.1 Å in the C-Na/N-Na RDFs (Figure 6.4b-c). However, when entering a neighboring subcube, the C-Na/N-Na RDFs deviate significantly. Since nitrogen stretches away from its associated iron and also moves more due to the weaker bonding character, this results in a disordered correlation (broad distribution) between sodium and nitrogen, while there is a more ordered correlation to carbon. Sodium is mainly distributed along *c* up to ±2.5 Å from its average position (Figure 6.4d), which is two and a half times more than its distribution along the two other directions.

In summary, the structure of iron- and sodium-based PBAs contains more nuanced disorder than the average structure suggests. Both the hydrated and dehydrated materials exhibit distortions of the nitrogen-bound iron octahedra, while the carbon-bound octahedra remain rigid. The distribution of sodium differs between the two samples, with more disorder in the dehydrated material. This is because there is no water present to keep the framework open and/or constrain the position of sodium within the PBA framework. However, even in the hydrated framework, sodium can take multiple positions if no water molecule blocks its pathway. This is in contrast to the analysis based on only the average structure, where sodium is seen to occupy the center of the PBA subcube. Therefore, the results suggest that the material is more dynamic than implied by the average structure. The distribution of the sodium also affects the orientation of the water molecules in the different phases. There is orientational order of the water molecules in the $P2_1/n$ phase and no orientational order in the $R\bar{3}$ phase due to increased mobility of both species at this temperature. Thus, these results show that the sodium distribution changes both between different hydrated phases but also when the material is dehydrated. All this can affect the sodium conduction pathways during cycling in a battery. In addition, if water is to be replaced with another small guest molecule, local interactions with the sodium need to be considered for its applications.

7. Dynamics of water

As evidenced by the diffraction results in Chapters 5 and 6, the water is not static. In fact, it has a very disordered nature that evolves with temperature, indicating dynamics. Neutron spectroscopy was applied in Papers IV and V to investigate the dynamics of the water in two samples. One sample had a high sodium and water content, while the other sample had a low sodium and water content ($Na_{1.90(9)}Fe^{2+}_{0.90(7)}Fe^{3+}_{0.10(3)}[Fe^{2+}(CN)_6]\cdot 2.12(2)H_2O$ and $Na_{0.34(5)}Fe^{3+}[Fe^{2.66(5)+}(CN)_6]\cdot 0.360(4)H_2O$, Table 3.1 Papers IV-V). The average structure for the low sodium sample determined by neutron diffraction showed that water occupies the center of each PBA subcube, while sodium is closer to the window faces. Since the desodiation is done without water present, sodium may be positioned closer to the cyanide ligands to obtain optimal bonding conditions, while water occupies the remaining space at the center of the subcube after rehydration.

7.1 Local diffusion

QENS was used to directly probe the reorientational dynamics of the water molecules in the temperature range 45 to 330 K. These temperatures were chosen to avoid water leaving the structure. Quasi-elastic broadening, originating from the hydrogen atoms in the water molecules, is observed for both samples in the investigated temperature range (Figure 7.1). There are still dynamics present at 45 K for both samples, which was the lowest temperature measured. The quasi-elastic broadening increases upon sodium

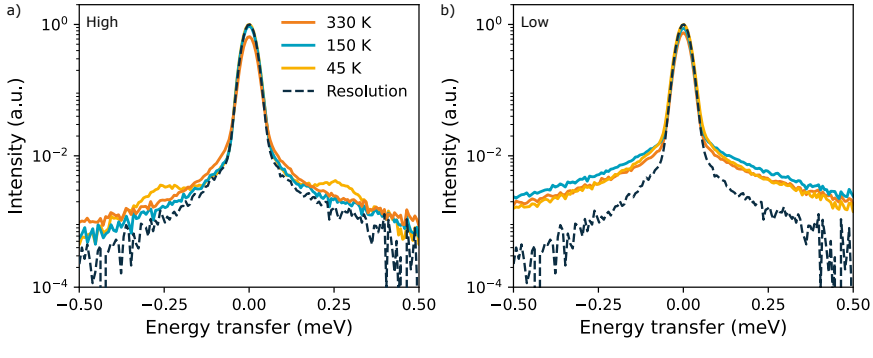

Figure 7.1. QENS spectra at 45, 150, and 330 K for the a) high sodium and b) low sodium samples.

removal, which could indicate faster dynamics in the sample with a low sodium content (Figure 7.1b). Two satellite peaks are observed in the QENS spectra in the temperature range 45 to 75 K for a high sodium content (Figure 7.1a), which is attributed to quantum rotational tunneling of the water with a small rotational energy barrier. Above 75 K, the tunneling peaks become part of the typical quasi-elastic broadening.

The spectra were fitted using two Lorentzians with two different widths (Figure 7.2), with both widths being independent of Q, suggesting localized dynamics. The area of the narrow Lorentzian (Lorentzian 1, slow dynamics) describes the majority of the scattered intensity, while the broad Lorentzian (Lorentzian 2, fast dynamics) was only ~6% of the area of the narrow Lorentzian, meaning that only a small part of the water contributes to the broad Lorentzian. This motion might be due to water being coordinated to sodium and performing a rattling motion or rotation around the 2-fold sodium-oxygen axis. This small fraction of the water is most likely the same water that, at lower temperatures, performs the quantum rotational tunneling since no broad component was found in the tunneling temperature range.

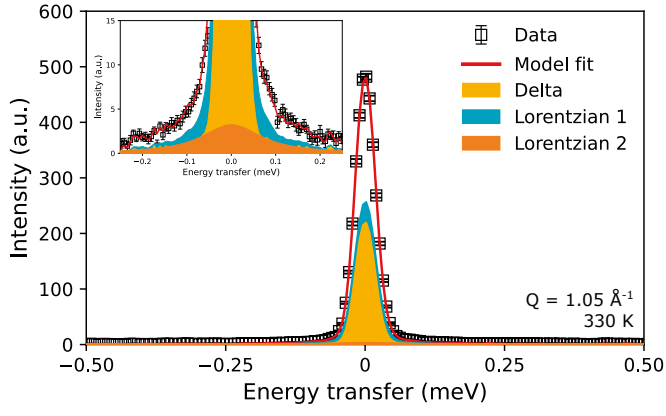

Figure 7.2. Representative fit of a QENS spectrum for the high sodium sample at 330 K (Q = 1.05 Å^{-1}) showing the individual components of the fit. The inset shows the broad Lorentzian 2. The error bars are one standard deviation.

Since local motion is present in the samples, the elastic incoherent structure factor (EISF) was determined and compared to different EISF models for water dynamics (Figure 7.3). The EISF describes the relation between the elastic and quasi-elastic contributions[1].

$$EISF = \frac{A_E(Q)}{A_E(Q) + \sum A_{QE,i}(Q)} \tag{7.1}$$

[1] $A_E(Q)$ is the area of the Delta function and $A_{QE,i}(Q)$ is the area of the Lorentzian functions.

The first EISF model describes the 2-fold rotation of the hydrogen atoms in a water molecule around the C_2-axis. The second EISF model describes an 8-fold rotation around the C_2-axis. The third EISF model describes the rotation of the hydrogen atoms around the oxygen atom that is fixed in the center. The fourth EISF model describes the diffusion of water within a spherical cavity with a specific radius. For both samples, the EISFs could be described using the spherical cavity model. For a high sodium content, the cavity radius was 2.6 Å. A cavity of such size could be found in the structure between two sodium atoms from two PBA subcubes. This agrees with the experimentally determined sodium-oxygen distance of 2.6 Å and the positional disorder described in Chapters 5 and 6. However, as seen in Chapter 6, these cavities might locally be positioned differently within the PBA framework than suggested by the average structure. Interestingly, the phase transition at room temperature does not affect the water dynamics even though the positional order of the water was lost during the phase transition (Chapter 5). For a low sodium content, a cavity of 1.8 Å was determined. In the structure of the low sodium sample, the sodium-oxygen distance is ~2.1 Å, however, the flexible PBA framework and the presence of sodium might

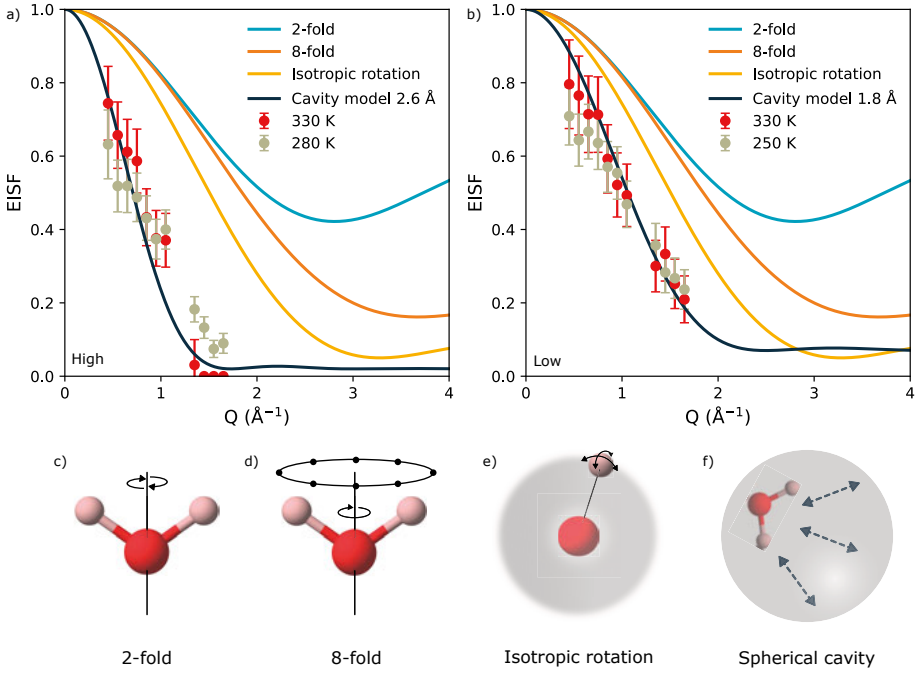

Figure 7.3. EISFs for a) high sodium at 280 and 330 K and b) low sodium at 250 and 330 K. The error bars are two standard deviations. Different EISF models for water. c) 2-fold rotation. d) 8-fold rotation. e) Isotropic rotation of hydrogen around the oxygen center. f) Spherical cavity with a specific radius.

result in a smaller effective cavity. This implies that sodium and water occupy each subcube simultaneously since the QENS and neutron diffraction data suggest a cavity smaller than if water were alone in a subcube. The water content was also seen to depend strongly on the sodium content in Chapter 4, where the water content especially decreased when the sodium content got below $x = 1$. The decreasing water content with decreasing sodium content suggests a strong interaction between sodium and water, which is in line with the observed co-existence of sodium and water in the low sodium sample.

In summary, the water in iron-based PBAs with varying sodium content exhibits localized dynamics with the water diffusing within a spherical cavity of a few Å matching the pore sizes within the structures as estimated from neutron diffraction. There is no difference in the water dynamics despite the phase transition from $P2_1/n$ to $R\bar{3}$ at room temperature. The insertion of sodium does not seem to affect the movement of water since the cavity size is similar to the vacancy-rich Prussian blue [4], however, the dynamics are significantly slowed down. The diffusion within cavities contributes to the stabilizing effect that water has on the PBA framework by keeping the framework enlarged. A small fraction of the water was found to bind to sodium, which is undesirable from an application point of view, since there is a risk of water removal during battery cycling. These results suggest that if one wants to replace water with another small molecule for battery applications, the new guest molecule does not require any specific geometry but must exhibit similar localized diffusion without binding tightly to sodium to ensure structural stability.

7.2 Vibrational dynamics

INS was used to probe water's interaction with sodium and the PBA framework in the temperature range 5 to 330 K. At 5 K, the $P2_1/n$ phase exists for the high sodium sample, while the low sodium sample has a $Fm\bar{3}m$ phase. For the sample with a high sodium content, well-defined peaks are present in the spectrum (Figure 7.4a) indicating well-defined local water environments. This is expected since the PBA framework is filled with water and sodium, thereby creating very similar water environments. When the sodium content is lowered, the INS spectrum becomes broader indicating a large distribution of local water environments. Since the sodium and water content is lower, there are many possible local water environments, *i.e.*, within one PBA subcube, sodium and water can co-exist, sodium can be alone, water can be alone, and/or the subcube can be completely empty. The intensity of the peaks is also affected by the lower water content relative to the high sodium sample. The water-related vibrations at ~1600 and ~3600 cm^{-1} are present in both samples but shift towards higher frequen-

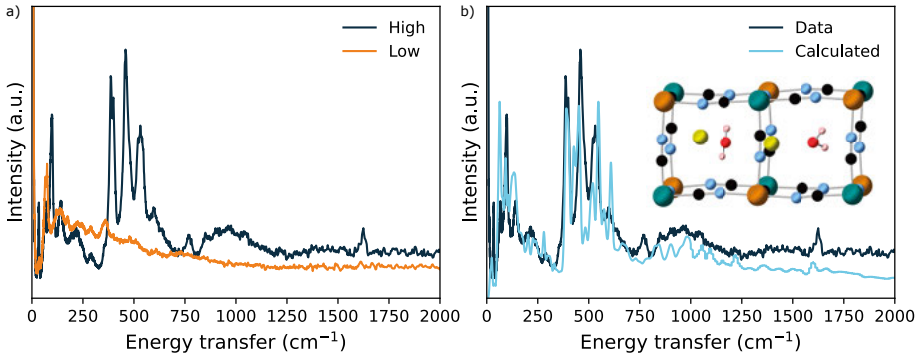

Figure 7.4. a) INS spectra for samples with a high and low sodium content measured at 10 K. b) Calculated INS spectrum based on the model with different sodium and water positions. The inset shows a cutout of the structural model. Carbon is shown in black, low-spin iron in green, high-spin iron in brown, nitrogen in blue, sodium in yellow, oxygen in red, and hydrogen in pale pink.

cies when less sodium is present due to less interaction with the sodium [58]. In addition, peaks a ~2100 cm^{-1} confirm the strong influence of water on the thermal expansion discussed in Chapter 5. That is, the presence of water affects the stretching of the cyanide and, consequently, the thermal expansion behavior in these materials. The temperature evolution of the INS spectra for the high sodium sample showed minor changes apart from broadening due to increased thermal motion. This indicates that the water environments in the $P2_1/n$ and $R\bar{3}$ phases are similar, as observed in Chapter 6.

To obtain more detailed information about the local water environments in the samples, calculated INS spectra based on different structural models were made and compared to the data. For a high sodium content, there is no consensus about the position of sodium and water within the PBA framework in the literature. Theoretical studies suggest that sodium is close to the window faces, while water occupies the center of the subcube [59, 60]. On the other hand, diffraction studies suggest that sodium occupies the center of the subcube, while water is on the window faces [21, 61]. This structural discrepancy is not seen for samples with a low sodium content [20, 47]. The advantage of INS is that it is a local probe of only the water, and therefore, the water can be separated from the other elements, unlike in total scattering, where the local structure is probed considering all the elements present. Calculated INS spectra based on structural models with either sodium at the center (with water on the window face) or sodium on the window face (with water in the center) could not describe the data well. A third model containing sodium and water at different positions describes the data well with most features in the spectra accounted for (Figure 7.4b). This model has most of the water (75%) in the center of the subcube, while a

small fraction is located close to the window faces. The different positions of sodium agree with the observations from the total scattering study in Chapter 6. The model with mixed sodium and water positions was applied to the low temperature neutron diffraction data and revealed that neutron diffraction alone is insufficient in differentiating the position of water and sodium. For a low sodium content, two different models were tested. One model has sodium and water co-existing within a subcube, while the other model has water alone within a subcube. The calculated INS spectra can describe several of the peaks in the spectrum, but there are still peaks that the model does not describe. Thus, the results suggest that there are several different local water environments present, and further theoretical calculations are needed to fully understand the low sodium PBA.

These results further confirm the disorder in these materials and that the position of sodium and water is more complex than previously suggested from diffraction and theoretical studies. Thus, local structural characterization using multiple techniques is crucial for understanding these materials. With this knowledge, better theoretical studies exploring the ionic transport in PBAs can be made.

8. Conclusions

This thesis explored the position of water and its dynamics as a function of the sodium content in iron-based, $[Fe(CN)_6]^{n-}$ vacancy-free PBAs. This has been achieved using different neutron scattering techniques probing different parts of the PBA. It was demonstrated that iron- and sodium-based PBAs are more complex than previously thought, and the supposed position of sodium and water within the PBA framework has been re-evaluated.

The different characterization techniques, probing both the average and local structure, have given different structural models for the material. Initially, water was thought to induce phase transitions, but this work shows that, in fact, water does not affect phase transitions but instead modifies the magnitude of the existing octahedral tilts within a given symmetry. The phase transitions are instead related to changes in the tilting of the iron octahedra. The tilt pattern can be affected by the position of sodium and water, as the ordering of sodium and water changes during phase transitions. However, the ordering of sodium and water in different phases might also be related to the specific tilt pattern of the iron octahedra given by the symmetry. In addition, bond length elongation and bond angle bending of the nitrogen-bound iron octahedra are an inherent property of these materials, which is challenging to describe from the average structure. Furthermore, this work shows that the loss of capacity from extensive battery cycling of the dehydrated material depends a lot less on the phase transition than initially expected. Instead, it is more important to optimize the loss of sodium in the battery system, and thereby prevent performance worsening. Thus, the PBA framework is flexible but retains structural integrity during sodium extraction/insertion and temperature changes.

The relationship between sodium and water proved to be more complicated. This work shows that the water is trapped inside cavities of a few Å matching the pore sizes in between the PBA framework and sodium. However, where these cavities are located within the PBA framework depends on the local positions of sodium and water, which change with temperature and composition. This work shows that both the center and window positions are possible for sodium, but there is a preference for the center position. However, there is a broad distribution of sodium between these two positions. Neutron diffraction was found to be insufficient in fully distinguishing these two positions, and local probes are therefore crucial to apply. The window position of sodium is achieved if there is no water molecule blocking the site, which consequently opens space at the center of the subcube for the water to occupy. On the other hand, the ordering of the sodium

affects the orientation of the water molecules, with the orientational order becoming less during heating. Thus, the relationship between sodium and water seems to be co-dependent, and they affect each other's position and orientation. The distribution of sodium is more disordered if no water is present. A lower sodium content also results in more disorder, as several local sodium and water environments are present in the material. A small fraction of the water was found to be directly coordinated to sodium, which is undesired from the point of view of battery applications since there is a risk of water removal over time.

Thus, the overall conclusion is that the iron- and sodium-based PBAs are more dynamic than previously thought. The knowledge obtained in this thesis opens up possible paths for substituting water with another molecule better suited for battery applications. The largest issue with replacing water is the practical implementation of a new guest molecule. Yet, the diversity of PBAs has proved that nothing is impossible.

9. Populärvetenskaplig sammanfattning

Preussiskt blått har varit känt sedan 1700-talet och ett flertal föreningar har framställts som baseras på preussiskt blått. Denna ansamling av föreningar går under namnet Preussisk-Blå-Analoger (PBA) och har många tillämpningar som sträcker sig från färgpigment till energilagring. PBAer har den generella sammansättningen $A_xM[M'(CN)_6]_{1-y}\cdot zG$ där *A* är en alkalimetall, *y* är antalet hexacyanojärnvakanser, *M* och *M'* är övergångsmetaller. Trots att föreningarna länge varit kända så finns det fortfarande en hel del som inte är känt kring hur den kemiska sammansättningen och kristallstrukturen hos PBAer påverkar deras egenskaper. Då PBAer innehåller cyanidjoner så finns det även en risk att materialen kan reagera med omgivningen och bilda giftig cyanidgas. Då järnbaserade PBAer generellt är mycket stabila så reagerar de inte med omgivningen och avger därmed inte cyanidgas. På grund av detta så ligger mycket fokus på just järnbaserade PBAer både för applikationer men också inom forskningen. En speciellt intressant PBA för batteritillämpningar är den järn- och natriumbaserade analogen med den kemiska sammansättningen $Na_{2-4y-x}Fe[Fe(CN)_6]_{1-y}\cdot zH_2O$. För att kunna anpassa egenskaperna hos denna grupp av material måste man först förstå hur sammansättningen, kristallstrukturen och vattendynamiken påverkar de relevanta egenskaperna. För att kunna börja relatera egenskaperna till dessa så behövs strategier för att med hög precision bestämma sammansättningen, strukturen och vattendynamiken vilket är vad den här avhandlingen fokuserar på. Avhandlingen nyttjar en stor mängd analysmetoder, men har haft ett extra fokus på neutronspridningsmetoder som är väldigt känsliga mot exempelvis vätet i en vattenmolekyl och är därför extra lämpade för studier av dessa PBAer.

Det är sen tidigare känt att antalet hexacyanojärnkomplex i PBA strukturen bestämmer hur mycket natrium och vatten som strukturen kan innehålla. Det är därför av yttersta vikt att bestämma om det finns såkallade hexacyanojärnvakanser, det vill säga antalet platser i strukturen där det saknas hexacyanojärnkomplex. PBAer innehåller två typer av järn, ett järn som tillhör hexacyanojärnkomplexet och ett "fritt" järn, det är därför svårt eller helt enkelt inte möjligt för många analysmetoder att fastställa antalet vakanser av hexacyanojärnkomplexen med någon högre precision. En metod som kan urskilja de två järnen är Mössbauerspektroskopi vilket gör det möjligt att bestämma antalet järnet som tillhör hexacyanojärnkomplexet och därmed vakanserna av komplexet. I denna avhandling har Mössbauerspektroskopi tillsammans med ett antal andra karakteriseringstekniker använts

för att bestämma sammansättningen. Vidare visar resultaten att även om flera metoder kan ge indikationer på sammansättningen så är det nödvändigt att använda flera kompletterande karakteriseringstekniker för att bestämma den verkliga samansättningen.

Tidigare studier av strukturen hos PBA provor med sammansättningen $Na_2Fe[Fe(CN)_6]\cdot zH_2O$ har visat att det finns flera möjliga strukturer kring rumstemperatur. Det har spekulerats att förekomsten av strukturerna beror på vilken syntesmetod som använts. Med hjälp av neutron- och röntgendiffraktion så fastställdes det att det två tidigare observerade strukturerna existerar, men att det är temperaturen som avgör vilken struktur som är stabil och inte syntesmetoden. De två strukturerna existerar alltså vid olika temperaturer och mellan 30 och 40 °C så omvandlas strukturen från den ena varianten till den andra. I avhandlingen presenteras även resultat för prover med ett högt respektive lågt kristallvatteninnehåll samt prover med ett lågt natrium innehåll, vilka visar att cellparametarna och kristallstrukturen även beror på mängden kristallvatten och natrium.

En omdebatterad fråga för den järn- och natriumbaserade analogen med högt natriuminnehåll är var i strukturen som natrium och vatten faktiskt befinner sig. Tidigare experimentella och teoretiska studier har föreslagit två olika positioner där natrium antingen befinner sig nära delkubens mitt eller nära någon av delkubens sidor. Genom att använda sig av neutrondiffraktion, neutrontotalspridning samt neutronspektroskopi så visar denna avhandling att natrium och vatten kan anta ett stort antal positioner lokalt i kristallstrukturen och att dessa positioner påverkar orienteringen av vattenmolekylerna. Vidare visade resultaten att vattnet rör sig aktivt i små lokala hålrum som finns i strukturen men visade inga tecken på långväga diffusion av vattnet. Utöver detta så visade resultaten att när antingen natriuminnehållet och/eller vatteninnehållet sänks så ökar oordningen av kvarvarande natrium och vatten, vilket troligen påverkar natriumjontransporten i materialet.

Genom att studera elektrokemin och kristallstrukturen under laddning och urladdning av förenklade battericeller med en järn- och natriumbaserade PBA katod (utan vatten) så observerades att den primära förlusten av kapacitet hos dessa batterier uppstår under de första cyklerna och är relaterat till en förlust av tillgängligt natrium. Detta visar att det primärt är andra processer som huvudsakligen orsaker kapacitetsförlusten och inte sprickbildning eller liknande kopplade till de strukturella fasövergångarna som sker i samband med laddning och urladdning.

Sammanfattningsvis så kan man säga att den här avhandlingen lägger grunden för vidare studier av hur egenskaperna hos PBAer beror på sammansättning, kristallstruktur och vattendynamik. Avhandlingen är därför ett viktigt steg i att förbättra möjligheterna för PBAer att användas som katodmaterial inom batteritillämpningar för att lagra energi men även för andra tillämpningar.

10. Acknowledgments

It is hard to believe that four years have passed, as it feels like just yesterday that I first came to Uppsala. But, as one says, time flies when you have fun, and that is what I have had a lot of!

To my supervisor **Mikael A.** I am very grateful that you joined the team. You have been an important part of the journey and have helped me in every way. I appreciate your ability to understand me, because I know it can be hard sometimes (especially when I have a potato in my mouth). Thanks for guiding and supporting me - I would not have gotten through this journey without you! To **Matt T.** Though not a supervisor on paper, you have been very important for my PhD. You are a big inspiration to me and I have enjoyed every moment working with you! Thanks to you and your group for being a second family in Oak Ridge. My time there has been priceless and I truly hope to return. To my supervisor **William B.** I have learned so much from you both about science but also about myself, and for that I am grateful. Thanks for allowing me to stay away from the lab, and for never saying no to my travels and ideas. To my supervisor **Maths K.** We have not interacted much during my PhD, but you have been a wise professor on the side. Thanks for always helping me when I have reached out.

A few people have become very special to me. **Casimir M.** I am so grateful that we became desk-buddies on day one. Your laugh, positivity, and fun company have made this journey so much more enjoyable! Thanks for being an amazing friend - I cannot wait to be friends for the next many years. Vi snakkes ved! **Agnes M.** I could not have gone through this crazy journey without you by my side to listen and always tell me how proud you are of me. Thanks for always being there for me, whether it was for fika, gossip, mental breakdowns, or big accomplishments. Remember to never go down on equipment! **Jonas H.** You are the most Swedish person I know, but despite that I have come to care a lot for you. You are a true friend and the best climbing buddy. Thanks for all the great adventures we have had. I promise that I will never drop you again! **Aram H.** Thanks for being the calm in my chaos and for always giving me hugs (and food) when I needed it the most. You are simply the best! **Babsi O.** When I found you, I felt a bit more at home here in Sweden. Thanks for all the herbal (witchcraft) tea for my weak stomach and your endless support. You are an amazing friend, and I know that you will always be there for me.

To **SwedNess.** I would not have enjoyed my PhD this much without the opportunities you have given me (in fact, it would have been rather boring!).

I have met so many amazing neutron people across the world, which has been lots of fun, but has also played a career-defining role for my future adventures. I have also gained an additional family. Thanks to all my fellow SwedNess people, especially the neutron besties! Traveling the world with you has been amazing, and I will never forget all of our fun trips. Cheers to keeping the memes good and our relationship strong wherever we go!

My PhD has also been influenced by many other people, both in Sweden and from around the world. **Alexandra U.** I am happy that I got to work with you! I would not have trusted any other person with my samples and sample preparation. You are golden (Au)! **Gustav E.** Thanks for being my diffraction go-to, co-parent to the stoe, sticky toffee pudding kompis, and for joining many of my beamtimes. It has been very hyggeligt! **Martin S.** Thanks for introducing me to climbing and for supporting me when I needed it. You are great at pushing me to do better every time. It has also been refreshing to have someone to speak Danish to when I sometimes got a bit tired of Sweden. **Daniel R.** After much effort from Martin S. (because we both go to the gym), we finally became friends after the Christmas party in 2023. It was refreshing to find a friend who is a bit more like me. Thanks for always believing in my dreams when no one else did and for encouraging me to lift heavier at the gym. I look back on many great times here and in Austria. **Valentin N.** Thanks for always being available for a chat. I appreciate that I can be my true self with you and that nothing is too weird to be discussed with you. Vi ses i København! **Meghdad H.** Thanks for a great reel-ationship and for helping me with my thesis cover! **Borges L., Ramon Z., Dayton K., Maksim E., Sylwia P., and Natasha C.** Thanks for making Oak Ridge a special place for me. I will definitely be back for more fun! **Alexis W.** Tack för att du har utmanat mig varje helg (även när jag var jättebakis), tävlat med (och mot) mig, spelat min favoritmusik och tagit hand om mig på Vanheim. Din energi är exceptionell! Kommer ihåg alla våra galna, men roliga ideer. Jag är alltid redo för ett handstand walk race med dig! **David R.** Du var min første ven her i Uppsala. Tak for at tage godt imod mig og få det til at føles som et hjem her. Jeg savner dig som min nabo og alle goderne, der fulgte med det (fika ved døren). Kom så!

Til min kære **familie og venner** i Danmark. Tak for at være med på denne rejse. Uden jeres støtte ville jeg ikke være her i dag! De sidste fire år er gået hurtigt og jeg er sikker på, at de næste to år i Schweiz også kommer til at gå hurtigt. Jeg kan ikke love, hvornår jeg kommer hjem igen, men jeg ved, at I altid er med mig uanset, hvor jeg er. Til min yndlings mule **Lya.** At komme hjem til dit søde og skøre væsen er det bedste jeg ved! Tak for alle de gode ture, vi har haft sammen ♡

Bibliography

[1] J. Woodward, Phil. Trans., 15–17 (1724).

[2] J. F. Keggin and F. D. Miles, "Structrue and Formulæ of the Prussian Blues and Related compounds", Nature **137**, 577–578 (1936).

[3] M. J. P. Munos and E. C. Martinez, *Prussian Blue Based Batteries* (Springer Cham, 2018), pp. 9–21.

[4] V. K. Sharma, S. Mitra, N. Thakur, S. M. Yusuf, F. Juranyi, and R. Mukhopadhyay, "Dynamics of water in prussian blue analogues: Neutron scattering study", J. Appl. Phys. **116**, 1–9 (2014).

[5] J. Long, Y. Guari, C. Guérin, and J. Larionova, "Prussian blue type nanoparticles for biomedical applications", Dalt. Trans. **45**, 17581–17587 (2016).

[6] B. Wang, Y. Han, X. Wang, N. Bahlawane, H. Pan, M. Yan, and Y. Jiang, "Prussian Blue Analogs for Rechargeable Batteries", iScience **3**, 110–133 (2018).

[7] E. S. Koumousi, I. R. Jeon, Q. Gao, P. Dechambenoit, D. N. Woodruff, P. Merzeau, L. Buisson, X. Jia, D. Li, F. Volatron, C. Mathonière, and R. Clérac, "Metal-to-metal electron transfer in Co/Fe prussian blue molecular analogues: The ultimate miniaturization", J. Am. Chem. Soc. **136**, 15461–15464 (2014).

[8] R. L. Germscheidt, D. Da Silva Francischini, M. B. Silva, M. A. Zezzi Arruda, A. L. Barboza Formiga, T. C. Rizuti Da Rocha, and J. A. Bonacin, "Water Oxidation Performance Enhanced by Electrochemically Designed Vacancies on a Prussian Blue Catalyst", ACS Appl. Energy Mater. **5**, 9447–9454 (2022).

[9] L. Reguera, C. P. Krap, J. Balmaseda, and E. Reguera, "Hydrogen storage in copper prussian blue analogues: Evidence of H_2 coordination to the copper atom", J. Phys. Chem. C **112**, 15893–15899 (2008).

[10] J. A. Dean, *Lange's Handbook of Chemistry*, edited by J. A. Dean, Fifteenth Ed. (New York, 1979).

[11] H. L. B. Boström and W. R. Brant, "Octahedral tilting in Prussian blue analogues", J. Mater. Chem. C **10**, 13690–13699 (2022).

[12] S. Adak, L. L. Daemen, M. Hartl, D. Williams, J. Summerhill, and H. Nakotte, "Thermal expansion in 3d-metal Prussian Blue Analogs - A survey study", J. Solid State Chem. **184**, 2854–2861 (2011).

[13] J. Roque, E. Reguera, J. Balmaseda, J. Rodríguez-Hernández, L. Reguera, and L. F. del Castillo, "Porous hexacyanocobaltates(III): Role of the metal on the framework properties", Microporous Mesoporous Mater. **103**, 57–71 (2007).

[14] A. L. Goodwin, K. W. Chapman, and C. J. Kepert, "Guest-dependent negative thermal expansion in nanoporous prussian blue analogues $M^{II}Pt^{IV}(CN)_6{\cdot}xH_2O$ ($0 \leq x \leq 2$; M = Zn, Cd).", J. Am. Chem. Soc. **127**, 17980–17981 (2005).

[15] D. Boras, I. Nielsen, A. Buckel, T. Ericsson, L. Häggström, R. Younesi, T. Stabb, and W. R. Brant, "Determening internal porosity in Prussian blue analogue cathode materials using poistron annihilation lifetime spectroscopy", J. Mater. Sci. **58**, 16344–16356 (2023).

[16] W. R. Brant, R. Mogensen, S. Colbin, D. O. Ojwang, S. Schmid, L. Häggström, T. Ericsson, A. Jaworski, A. J. Pell, and R. Younesi, "Selective Control of Composition in Prussian White for Enhanced Material Properties", Chem. Mater. **31**, 7203–7211 (2019).

[17] D. O. Ojwang, M. Svensson, C. Njel, R. Mogensen, A. S. Menon, T. Ericsson, L. Häggström, J. Maibach, and W. R. Brant, "Moisture-Driven Degradation Pathways in Prussian White Cathode Material for Sodium-Ion Batteries", ACS Appl. Mater. Interfaces **13**, 10054–10063 (2021).

[18] D. O. Ojwang, L. Häggström, T. Ericsson, R. Mogensen, and W. R. Brant, "Guest water hinders sodium-ion diffusion in low-defect Berlin green cathode material", Daltron Trans. **51**, 14712–14720 (2022).

[19] A. Rudola, K. Du, and P. Balaya, "Monoclinic Sodium Iron Hexacyanoferrate Cathode and Non-Flammable Glyme-Based Electrolyte for Inexpensive Sodium-Ion Batteries", J. Electrochem. Soc. **164**, A1098–A1109 (2017).

[20] X. Guo, Z. Wang, Z. Deng, X. Li, B. Wang, X. Chen, and S. P. Ong, "Water Contributes to Higher Energy Density and Cycling Stability of Prussian Blue Analogue Cathodes for Aqueous Sodium-Ion Batteries", Chem. Mater. **31**, 5933–5942 (2019).

[21] I. Nielsen, D. Dzodan, D. O. Ojwang, P. F. Henry, A. Ulander, G. Ek, L. Häggström, T. Ericsson, H. L. B. Boström, and W. R. Brant, "Water driven phase transitions in Prussian White cathode materials", J. Phys. Energy **4**, 044012 (2022).

[22] I. Nielsen, A. Ulander, F. Juranyi, S. R. Larsen, M. Karlsson, W. R. Brant, and M. S. Andersson, "Impact of Sodium on the Water Dynamics in Prussian Blue Analogues", Chem. Mater. **36**, 11246–11253 (2024).

[23] C. J. Carlile and B. T. M. Willis, *Experimental neutron scattering* (Oxford University Press, 2009).

[24] J. Pannetier, *Neutron and Synchrotron Radiation for Condensed Matter Studies*, edited by J. Baruchel, J. L. Hodeau, M. S. Lehmann, J. R. Regnard, and C. Schlenker, Vol. 1 (Les Editions De Physique. Springer-Verlag, 1994).

[25] H. M. Rietveld, "A profile refinement method for nuclear and magnetic structures", J. Appl. Crystallogr. **2**, 65–71 (1969).

[26] B. H. Toby, "R factors in Rietveld analysis: How good is good enough?", Powder Diffr. **21**, 67–70 (2006).

[27] A. C. Dippel, H. P. Liermann, J. T. Delitz, P. Walter, H. Schulte-Schrepping, O. H. Seeck, and H. Franz, "Beamline P02.1 at PETRA III for high-resolution and high-energy powder diffraction", J. Synchrotron Radiat. **22**, 675–687 (2015).

[28] R. I. Smith, S. Hull, M. G. Tucker, H. Y. Playford, D. J. McPhail, S. P. Waller, and S. T. Norberg, "The upgraded Polaris powder diffractometer at the ISIS neutron source", Rev. Sci. Instrum. **90** (2019).

[29] J. Neuefeind, M. Feygenson, J. Carruth, R. Hoffmann, and K. K. Chipley, "The Nanoscale Ordered MAterials Diffractometer NOMAD at the Spallation Neutron Source SNS", Nucl. Instruments Methods Phys. Res. Sect. B Beam Interact. with Mater. Atoms **287**, 68–75 (2012).

[30] A. A. Coelho, "TOPAS and TOPAS-Academic: An optimization program integrating computer algebra and crystallographic objects written in C++", J. Appl. Crystallogr. **51**, 210–218 (2018).

[31] *Images and video generated using CrystalMaker®: a crystal and molecular structures program for Mac and Windows. CrystalMaker Software Ltd, Oxford, England.*

[32] S. J. L. Billinge and K. M. Ø. Jensen, *Atomic pair distribution function analysis: a primer* (Oxford University Press, 2023).

[33] D. A. Keen, "A comparison of various commonly used correlation functions for describing total scattering", J. Appl. Crystallogr. **34**, 172–177 (2001).

[34] C. L. Farrow, P. Juhas, J. W. Liu, D. Bryndin, E. S. Boin, J. Bloch, T. Proffen, and S. J. Billinge, "PDFfit2 and PDFgui: Computer programs for studying nanostructure in crystals", J. Condens. Matter Phys. **19**, 335219 (2007).

[35] M. G. Tucker, D. A. Keen, M. T. Dove, A. L. Goodwin, and Q. Hui, "RMCProfile: Reverse Monte Carlo for polycrystalline materials", J. Phys. Condens. Matter **19** (2007).

[36] Y. Zhang, M. Eremenko, V. Krayzman, M. G. Tucker, and I. Levin, "New capabilities for enhancement of RMCProfile: Instrumental profiles with arbitrary peak shapes for structural refinements using the reverse Monte Carlo method", J. Appl. Crystallogr. **53**, 1509–1518 (2020).

[37] S. F. Parker, D. Lennon, and P. W. Albers, "Vibrational spectroscopy with neutrons: A review of new directions", Appl. Spectrosc. **65**, 1325–1341 (2011).

[38] S. F. Parker, C. J. Carlile, T. Pike, J. Tomkinson, R. J. Newport, C. Andreani, F. P. Ricci, F. Sacchetti, and M. Zoppi, "TOSCA: a world class inelastic neutron spectrometer", Phys. B Condens. Matter **241-243**, 154–156 (1997).

[39] S. F. Parker, F. Fernandez-Alonso, A. J. Ramirez-Cuesta, J. Tomkinson, S. Rudic, R. S. Pinna, G. Gorini, and J. Fernández Castañon, "Recent and future developments on TOSCA at ISIS", J. Phys. Conf. Ser. **554** (2014).

[40] R. A. Ewings, J. R. Stewart, T. G. Perring, R. I. Bewley, M. D. Le, D. Raspino, D. E. Pooley, G. Škoro, S. P. Waller, D. Zacek, C. A. Smith, and R. C. Riehl-Shaw, "Upgrade to the MAPS neutron time-of-flight chopper spectrometer", Rev. Sci. Instrum. **90** (2019).

[41] P. A. Seeger, L. L. Daemen, and J. Z. Larese, "Resolution of VISION, a crystal-analyzer spectrometer", Nucl. Instruments Methods Phys. Res. Sect. A Accel. Spectrometers, Detect. Assoc. Equip. **604**, 719–728 (2009).

[42] Y. Q. Cheng, L. L. Daemen, A. I. Kolesnikov, and A. J. Ramirez-Cuesta, "Simulation of Inelastic Neutron Scattering Spectra Using OCLIMAX", J. Chem. Theory Comput. **15**, 1974–1982 (2019).

[43] Y. Q. Cheng, A. I. Kolesnikov, and A. J. Ramirez-Cuesta, "Simulation of Inelastic Neutron Scattering Spectra Directly from Molecular Dynamics Trajectories", J. Chem. Theory Comput. **16**, 7702–7708 (2020).

[44] N. Verdal, T. J. Udovic, J. J. Rush, V. Stavila, H. Wu, W. Zhou, and T. Jenkins, "Low-temperature tunneling and rotational dynamics of the ammonium cations in $(NH_4)_2B_{12}H_{12}$", J. Chem. Phys. **135**, 2–10 (2011).

[45] S. Janßen, J. Mesot, L. Holitzner, A. Furrer, and R. Hampelmann, "FOCUS: A hybrid TOF-spectrometer at SINQ", Phys. B Condens. Matter **234-236**, 1174–1176 (1997).

[46] R. T. Azuah, L. R. Kneller, Y. Qiu, P. L. Tregenna-Piggott, C. M. Brown, J. R. Copley, and R. M. Dimeo, "DAVE: A comprehensive software suite for the reduction, visualization, and analysis of low energy neutron spectroscopic data", J. Res. Natl. Inst. Stand. Technol. **114**, 341–358 (2009).

[47] D. O. Ojwang, L. Häggström, T. Ericsson, J. Angström, and W. R. Brant, "Influence of sodium content on the thermal behavior of low vacancy Prussian white cathode material", Dalt. Trans. **49**, 3570–3579 (2020).

[48] C. Aparicio, L. Machala, and Z. Marusak, “Thermal decomposition of Prussian blue under inert atmosphere”, J. Therm. Anal. Calorim. **110**, 661–669 (2012).

[49] J. Banhart, M. D. Lay, C. S. Chang, and A. J. Hill, “Kinetics of natural aging in Al-Mg-Si alloys studied by positron annihilation lifetime spectroscopy”, Phys. Rev. B - Condens. Matter Mater. Phys. **83**, 014101 (2011).

[50] P. S. Camacho, R. Wernert, M. Duttine, A. Wattiaux, A. Rudola, P. Balaya, R. Berthelot, L. Monconduit, D. Carlier, and L. Croguennec, “Impact of Synthesis Conditions in Na-Rich Prussian Blue Analogues”, ACS Appl. Mater. Interfaces **13**, 42682–42692 (2021).

[51] W. Wang, Y. Gang, J. Peng, Z. Hu, Z. Yan, W. Lai, Y. Zhu, D. Appadoo, M. Ye, Y. Cao, Q.-f. Gu, H.-k. Liu, S.-x. Dou, and S.-l. Chou, “Effect of Eliminating Water in Prussian Blue Cathode for Sodium-Ion Batteries”, Adv. Funct. Mater. **2111727**, 1–13 (2022).

[52] A. M. Glazer, “The classification of tilted octahedra in perovskites”, Acta Crystallogr. Sect. B Struct. Crystallogr. Cryst. Chem. **28**, 3384–3392 (1972).

[53] C. J. Howard, B. J. Kennedy, and P. M. Woodward, “Ordered double perovskites - A group-theoretical analysis”, Acta Crystallogr. Sect. B Struct. Sci. **59**, 463–471 (2003).

[54] K. W. Chapman, P. J. Chupas, and C. J. Kepert, “Compositional dependence of negative thermal expansion in the Prussian blue analogues $M^{II}Pt^{IV}(CN)_6$ (M = Mn, Fe, Co, Ni, Cu, Zn, Cd)”, J. Am. Chem. Soc. **128**, 7009–7014 (2006).

[55] N. Shi, Q. Gao, A. Sanson, Q. Li, L. Fan, Y. Ren, L. Olivi, J. Chen, and X. Xing, “Negative thermal expansion in cubic $FeFe(CN)_6$ Prussian blue analogues”, Dalt. Trans. **48**, 3658–3663 (2019).

[56] Q. Gao, N. Shi, A. Sanson, Y. Sun, R. Milazzo, L. Olivi, H. Zhu, S. H. Lapidus, L. Zheng, J. Chen, and X. Xing, “Tunable Thermal Expansion from Negative, Zero, to Positive in Cubic Prussian Blue Analogues of $GaFe(CN)_6$”, Inorg. Chem. **57**, 14027–14030 (2018).

[57] A. Buckel, C. A. Hall, L. A. Ma, L. O. Colbin, H. Eriksson, R. Mogensen, and R. Younesi, “Importance of First Cycle Conditions on the Electrochemical Performance of Hard Carbon and Prussian White Based Sodium-Ion Batteries Using Fire Resistant, Fluorine-Free Electrolyte”, Batter. Supercaps **202300533** (2023).

[58] F. Perakis, L. D. Marco, A. Shalit, F. Tang, Z. R. Kann, T. D. Kühne, R. Torre, M. Bonn, and Y. Nagata, “Vibrational Spectroscopy and Dynamics of Water”, Chem. Rev. **116**, 7590–7607 (2016).

[59] C. Ling, J. Chen, and F. Mizuno, “First-principles study of alkali and alkaline earth ion intercalation in iron hexacyanoferrate: The important role of ionic radius”, J. Phys. Chem. C **117**, 21158–21165 (2013).

[60] S. Liu and K. C. Smith, “Effects of interstitial water and alkali cations on the expansion, intercalation potential, and orbital coupling of nickel hexacyanoferrate from first principles”, J. Appl. Phys. **131**, 105101 (2022).

[61] J. Song, L. Wang, Y. Lu, J. Liu, B. Guo, P. Xiao, J. J. Lee, X. Q. Yang, G. Henkelman, and J. B. Goodenough, “Removal of Interstitial H_2O in Hexacyanometallates for a Superior Cathode of a Sodium-Ion Battery”, J. Am. Chem. Soc. **137**, 2658–2664 (2015).

Acta Universitatis Upsaliensis

Digital Comprehensive Summaries of Uppsala Dissertations from the Faculty of Science and Technology 2571

Editor: The Dean of the Faculty of Science and Technology

A doctoral dissertation from the Faculty of Science and Technology, Uppsala University, is usually a summary of a number of papers. A few copies of the complete dissertation are kept at major Swedish research libraries, while the summary alone is distributed internationally through the series Digital Comprehensive Summaries of Uppsala Dissertations from the Faculty of Science and Technology. (Prior to January, 2005, the series was published under the title "Comprehensive Summaries of Uppsala Dissertations from the Faculty of Science and Technology".)

Distribution: publications.uu.se
urn:nbn:se:uu:diva-565121

ACTA UNIVERSITATIS
UPSALIENSIS
2025